

# **Fine-scale Segmentation and Spatiotemporal Variability of the 2010 Mw 8.8 Maule Aftershock Sequence Revealed by a Deep-Learning-Based Earthquake Catalog**

**Rodrigo Flores-Allende<sup>1</sup>, Léonard Seydoux<sup>1</sup>, Éric Beaucé<sup>2,3</sup>, Luis Fabian Bonilla<sup>3,1</sup>,  
Philippe Gueguen<sup>4</sup> and Claudio Satriano<sup>1</sup>**

<sup>1</sup>Université Paris Cité, Institut de physique du globe de Paris, UMR 7154, Paris, France

<sup>2</sup>Lamont-Doherty Earth Observatory, Columbia University, New York, NY, USA

<sup>3</sup>Université Gustave Eiffel, Champs-sur-Marne, Marne-la-Vallée, France

<sup>4</sup>ISTerre, Université Grenoble Alpes/CNRS/Univ. Savoie Mont-Blanc/IRD/Université Gustave Eiffel,  
38000 Grenoble, France

**Corresponding author:** floresallende@ipgp.fr

## **Peer-review status:**

**This manuscript has been submitted to Journal of Geophysical Research: Solid Earth and is currently under review. It has not yet been formally accepted for publication. Subsequent versions of this manuscript may differ from this version.**

1 **Fine-scale Segmentation and Spatiotemporal Variability**  
2 **of the 2010  $M_w$  8.8 Maule Aftershock Sequence**  
3 **Revealed by a Deep-Learning-Based Earthquake**  
4 **Catalog**

5 **Rodrigo Flores-Allende<sup>1</sup>, Léonard Seydoux<sup>1</sup>, Éric Beaucé<sup>2</sup>,**  
6 **Luis Fabian Bonilla<sup>3,1</sup>, Philippe Gueguen<sup>4</sup> and Claudio Satriano<sup>1</sup>**

7 <sup>1</sup>Université Paris Cité, Institut de Physique du Globe de Paris, UMR 7154, Paris, France

8 <sup>2</sup>Lamont-Doherty Earth Observatory, Columbia University, New York, NY, USA

9 <sup>3</sup>Université Gustave Eiffel, Champs-sur-Marne, Marne-la-Vallée, France

10 <sup>4</sup>ISTerre, Université Grenoble Alpes/CNRS/Univ. Savoie Mont-Blanc/IRD/Université Gustave Eiffel,  
11 38000 Grenoble, France

12 **Key Points:**

13 • We build a dense catalog of 537,390 aftershocks of the 2010  $M_w$  8.8 Maule earthquake,  
14 achieving a completeness magnitude of about  $M_w$  1.8.

15 • Automated detection and relocation yield consistent magnitudes and improved loca-  
16 tions across variable network coverage.

17 • Spatial  $b$ -values vary along strike, consistent with a weaker, fluid-rich northern inter-  
18 face and a stronger southern megathrust.

19 **Abstract**

20 We re-examine the aftershock sequence of the  $M_w$  8.8 Maule earthquake in south-central  
 21 Chile to understand how seismicity, magnitude-frequency distribution, and fault structure  
 22 vary along the rupture zone. Using the International Maule Aftershock Deployment (IMAD)  
 23 dataset, we analyze ten months of continuous data from 156 temporary stations and build  
 24 a high-resolution aftershock catalog for the Maule rupture zone. We apply the BeamPower  
 25 and Matched Filtering (BPMF) workflow, which integrates a deep-learning phase picker  
 26 with backprojection-based association, relative relocation, and template matching. We ini-  
 27 tially detect and relocate 130,578 earthquakes, then use a subset of high-quality events as  
 28 templates to identify smaller earthquakes missed by the initial detection. The final catalog  
 29 contains about 537,390 earthquakes, nearly 13 times more than previous studies, with a  
 30 completeness magnitude of  $\sim M_w$  1.8 and magnitudes ranging from  $M_w$  0.2 to  $M_w$  6.2. A  
 31 regional local magnitude ( $M_L$ ) calibration ensures homogeneous magnitude scales across  
 32 the network. The dense catalog resolves detailed seismotectonic features along the rupture.  
 33 In the Pichilemu region, aftershocks delineate a shallow normal fault system with L-shaped  
 34 geometry, whereas the Concepción area exhibits aseismic patches. Using classical maximum  
 35 likelihood and  $b$ -more-incomplete methods, we find that temporal  $b$ -values range between 1.2  
 36 and 1.6 early in the sequence and converge toward about 1.0. Meanwhile, spatial  $b$ -values  
 37 are strongly segmented along strike, with higher values in the north and lower values in  
 38 the south. These contrasts are consistent with along-strike variations in effective stress and  
 39 pore fluid pressure on the plate interface, in line with previous studies.

40 **Plain Language Summary**

41 After a large earthquake, the Earth continues to adjust through thousands of smaller events  
 42 called aftershocks. Studying when and where these aftershocks occur helps scientists under-  
 43 stand how the fault releases stress and improves future hazard assessments. We revisit the  
 44 aftershocks of the 2010 magnitude 8.8 Maule earthquake in south-central Chile using nearly  
 45 a year of data from 156 temporary seismic stations. By applying modern computer-based  
 46 methods, including machine learning and template matching techniques, we detect and lo-  
 47 cate many small earthquakes that were not identified before. The new earthquake catalog  
 48 includes more than half a million events, about 13 times more than in previous studies,  
 49 and shows that aftershocks are not distributed evenly along the fault. Near Pichilemu, they  
 50 outline a shallow fault system, while deeper activity occurs within the oceanic plate that  
 51 is sinking beneath South America. We also examine how the proportion of small to large  
 52 earthquakes changes over time and along the fault, which provides clues about differences  
 53 in stress, fluid presence, and rock strength. This study demonstrates how advanced analysis  
 54 tools applied to existing data can reveal new details about how great earthquakes rupture  
 55 and how subduction zones evolve over time.

56 **1 Introduction**

57 On February 27, 2010, a  $M_w$  8.8 earthquake struck the Maule region in south-central  
 58 Chile, causing significant loss of life and widespread damage (Salazar & McNutt, 2011).  
 59 The rupture extended 500 km along the convergence margin between the Pacific and Nazca  
 60 plates, between latitudes 33°S and 38.5°S (Figure 1a). This event ranks among the largest  
 61 instrumentally recorded earthquakes worldwide, and is the strongest well-recorded in Chile  
 62 (e.g., Delouis et al., 2010; Madariaga et al., 2010; Moreno et al., 2010; Vigny et al., 2011;  
 63 S. Ruiz et al., 2012; Hicks et al., 2014; S. Ruiz & Madariaga, 2018). Its rupture coincides with  
 64 the mature seismic gap left by the  $M_w$  8.3 earthquake of 1835 (see, e.g., Campos et al., 2002),  
 65 and overlaps segments of previous major earthquakes, including the  $M_w$  7.7 Talca (1928),  
 66  $M_w$  8.1 Concepción (1960, e.g., Ojeda et al., 2020), and  $M_w$  7.8 Arauco (1975) earthquakes.  
 67 It also partially overlaps the  $M_w$  9.5 Valdivia earthquake area of 1960, the largest earthquake  
 68 ever recorded in history (e.g., Madariaga et al., 2010; S. Ruiz et al., 2012).

69 Large megathrust earthquakes, such as those related to subduction zones, are typically  
 70 followed by an increase in seismic activity known as aftershocks. Earthquakes are considered  
 71 aftershocks when their magnitude is at least one unit smaller than the mainshock (Båth,  
 72 1965), and can persist for weeks to years (Bilek & Lay, 2018). They result from stress per-  
 73 turbations induced by the main rupture (Felzer et al., 2004), and their distribution across  
 74 the rupture zone often correlates with regions of high postseismic strain and substantial  
 75 static stress changes (Lange et al., 2012; Rietbrock et al., 2012). Among the many after-  
 76 shocks of the Maule earthquake, shortly after the mainshock, two large aftershocks of  $M_w$   
 77 6.9 and  $M_w$  6.7 struck the area of Pichilemu on March 11, 2010, at the northern edge of the  
 78 rupture zone (Farías et al., 2011; Lange et al., 2012; Rietbrock et al., 2012; Ryder et al.,  
 79 2012; J. A. Ruiz et al., 2014; Jara-Muñoz et al., 2022). These aftershocks suggest a potential  
 80 migration of seismicity or the reactivation of analogous fault systems in the region.

81 Over the past decade, the International Maule Aftershock Deployment (IMAD) dataset  
 82 has been a key resource for studying the Maule aftershock sequence. Deployed within a few  
 83 weeks after the mainshock (Guéguen et al., 2011), this mobile seismic network covered  
 84 the entire rupture area (Figure 1a) and enabled the construction of some early earthquake  
 85 catalogs. For instance, Lange et al. (2012) and Rietbrock et al. (2012) applied classical  
 86 Short-Term Average to Long-Term Average (STA/LTA) automatic pickers, detecting over  
 87 20,000 events in six months and more than 30,000 events in just two months, respectively.  
 88 These initial efforts provided a broad overview of the rupture segmentation, aftershock dis-  
 89 tribution, and fault reactivation. Using the catalog from Rietbrock et al. (2012); Agurto et  
 90 al. (2012), they refined the locations of the largest aftershocks and performed regional mo-  
 91 ment tensor (RMT) inversions to characterize spatio-temporal variations in seismic moment  
 92 release. One of the main observations was the apparent lack of large aftershocks in regions  
 93 of highest coseismic slip (Agurto et al., 2012; Rietbrock et al., 2012). Although this pattern  
 94 appears to depend on the selected slip model, both studies agreed that only low-magnitude  
 95 seismicity was present in these high-slip patches. This emphasizes the need for accurate  
 96 detection and location of small events to delineate and characterize the interaction between  
 97 seismic and aseismic patches. As a result, the contribution of these regions to the total  
 98 postseismic deformation budget remains unclear, and deeper intraslab contributions may  
 99 also be underestimated. Moreover, Neighbors et al. (2015) estimated the high-frequency  
 100 attenuation parameter  $\kappa$ , finding significant spatial variability likely reflecting the combined  
 101 effects of source, path, and site conditions, though poorly correlated with surface geology. In  
 102 parallel, Tassara et al. (2016) analyzed  $b$ -value patterns in relation to afterslip and identified  
 103 contrasting mechanical domains along strike, which they related to variations in fluid con-  
 104 tent and fault rheology. While both studies provided valuable constraints, their resolution  
 105 was limited by the number of events used, as they considered only a few subsets of moderate-  
 106 to-large magnitude aftershocks. In this study, we build on these previous constraints using  
 107 a much denser, magnitude-calibrated aftershock catalog and a  $b$ -value estimator that is less  
 108 sensitive to completeness, which allows us to resolve the along-strike segmentation of the  
 109 Maule rupture and to reassess the role of fluids and effective normal stress in controlling  
 110 aftershock behavior.

111 A clear understanding of aftershock patterns, afterslip distribution, and triggering  
 112 mechanisms is key to improving our knowledge of earthquake mechanics (Peng & Zhao, 2009;  
 113 Yao et al., 2017; Minetto et al., 2022; Farge & Brodsky, 2025). Although often neglected in  
 114 stress-transfer models, small-magnitude earthquakes can collectively have a significant im-  
 115 pact due to their high occurrence and spatial clustering. Marsan (2005) demonstrated that  
 116 stress perturbations from small earthquakes can be as influential as those from larger ones,  
 117 highlighting the importance of including microseismicity in further analysis. For instance,  
 118 S. Ruiz et al. (2017) used repeaters to reveal aseismic processes before and after the 2017  
 119  $M_w$  6.9 Valparaíso earthquake, suggesting that small-scale seismicity may have triggered the  
 120 mainshock and played an important role in the rupture dynamics. However, current studies  
 121 mainly rely on large-magnitude aftershocks, as detecting smaller ones remains challenging.  
 122 Seismic noise often hinders the detection of low-magnitude aftershocks, particularly when

123 using traditional methods based on signal amplitude such as Signal-to-Noise Ratio (SNR)  
 124 or the previously mentioned STA/LTA trigger (see, e.g., Allen, 1982). Other factors, such  
 125 as wave scattering and attenuation, further complicate the detection of small aftershocks,  
 126 especially in regions with extensive rupture zones and sparse seismic networks as in the  
 127 present study (Figure 1b).

128 Recent advances in deep learning have significantly improved the quality of earthquake  
 129 catalogs (Ross et al., 2019; Mousavi & Beroza, 2023; Zhu & Beroza, 2019). These methods  
 130 excel at identifying low-magnitude events and provide more reliable locations, unveiling the  
 131 intricate details of seismic sequences and fault structures (Beaucé et al., 2019; Tan et al.,  
 132 2021; Beaucé et al., 2022; Mancini et al., 2022; Minetto et al., 2022). In this study, we use  
 133 these techniques to reassess an old, but distinctive dataset recorded by the IMAD network  
 134 (Beck et al., 2014). We build a high resolution earthquake catalog of the Maule aftershock  
 135 sequence and analyze how seismicity is distributed in space and time across the rupture  
 136 zone. Our goal is to resolve how aftershock distribution, magnitude statistics, and fault  
 137 structure vary along the Maule rupture zone, which remained only partially imaged in pre-  
 138 vious studies. We pursue three main objectives. First, we construct a dense and internally  
 139 consistent catalog under strongly variable station coverage, combining automatic phase pick-  
 140 ing, backprojection-based association, and two relocation stages, so that small earthquakes  
 141 can be used reliably to map fine-scale structures and stress heterogeneity. Second, we cali-  
 142 brate a regional local magnitude scale directly from Maule waveforms and reference moment  
 143 magnitudes, and use it to obtain homogeneous  $M_L$  and  $M_w$  for all events. Third, we map  
 144 spatial and temporal variations of the  $b$ -value and magnitude of completeness, and relate  
 145 these patterns to the segmented plate interface and to the Pichilemu crustal fault system.

146 To achieve this, we follow the BeamPower and Matched Filtering (BPMF) strategy of  
 147 Beaucé et al. (2024), combining the deep-neural-network seismic phase picking PhaseNet  
 148 (Zhu & Beroza, 2019) with backprojection (Frank & Shapiro, 2014) to detect and locate  
 149 earthquakes, and two relocation stages with NonLinLoc (Lomax, 2001; Lomax & Savvaïdis,  
 150 2022) to build an initial catalog. We then apply a template matching to these well located  
 151 events (Gibbons & Ringdal, 2006; Frank & Shapiro, 2014; Beaucé et al., 2018) to identify ad-  
 152 ditional earthquakes that would otherwise be missed by conventional techniques, increasing  
 153 the catalog completeness and extending the magnitude range (Minetto et al., 2022).

154 In the following sections, we first outline the tectonic context of south-central Chile,  
 155 with a focus on the 2010 Maule earthquake and its aftershock sequence. We then describe  
 156 the IMAD database and the BPMF method used for earthquake detection, association,  
 157 and relocation, and we summarize the resulting catalog. Next, we present the magnitude  
 158 calibration, derive homogeneous  $M_L$  and  $M_w$ , and perform a Gutenberg–Richter analysis,  
 159 including a recent method for estimating the  $b$ -value that is less sensitive to time-dependent  
 160 completeness. Finally, we analyze the spatiotemporal distribution of seismicity, compare  
 161 the new catalog to previous ones, and discuss the implications for rupture segmentation and  
 162 the Pichilemu fault system.

## 163 2 Geotectonic setting

164 The Maule segment of the south-central Chilean subduction zone (33–39°S) is a tec-  
 165 tonically transitional region that accommodates oblique convergence between the Nazca  
 166 and South American plates at approximately 66 mm/year (Haberland et al., 2009). This  
 167 segment is bounded by the subducted Juan Fernández Ridge to the north and the Mocha  
 168 Fracture Zone to the south, and marks a transition from a strongly coupled interface in  
 169 central Chile to a more weakly coupled regime farther south (Moreno et al., 2010; Vigny et  
 170 al., 2011). The segmentation is shaped by inherited lithospheric discontinuities, including  
 171 the Lanalhue Fault Zone and terrane boundaries across a metamorphic Paleozoic basement  
 172 intruded by Mesozoic granitoids (Hervé et al., 1987, 1988; Mpodozis & Ramos, 1990; Glodny  
 173 et al., 2008; Aron et al., 2015). These crustal features influence upper-plate faulting, forearc

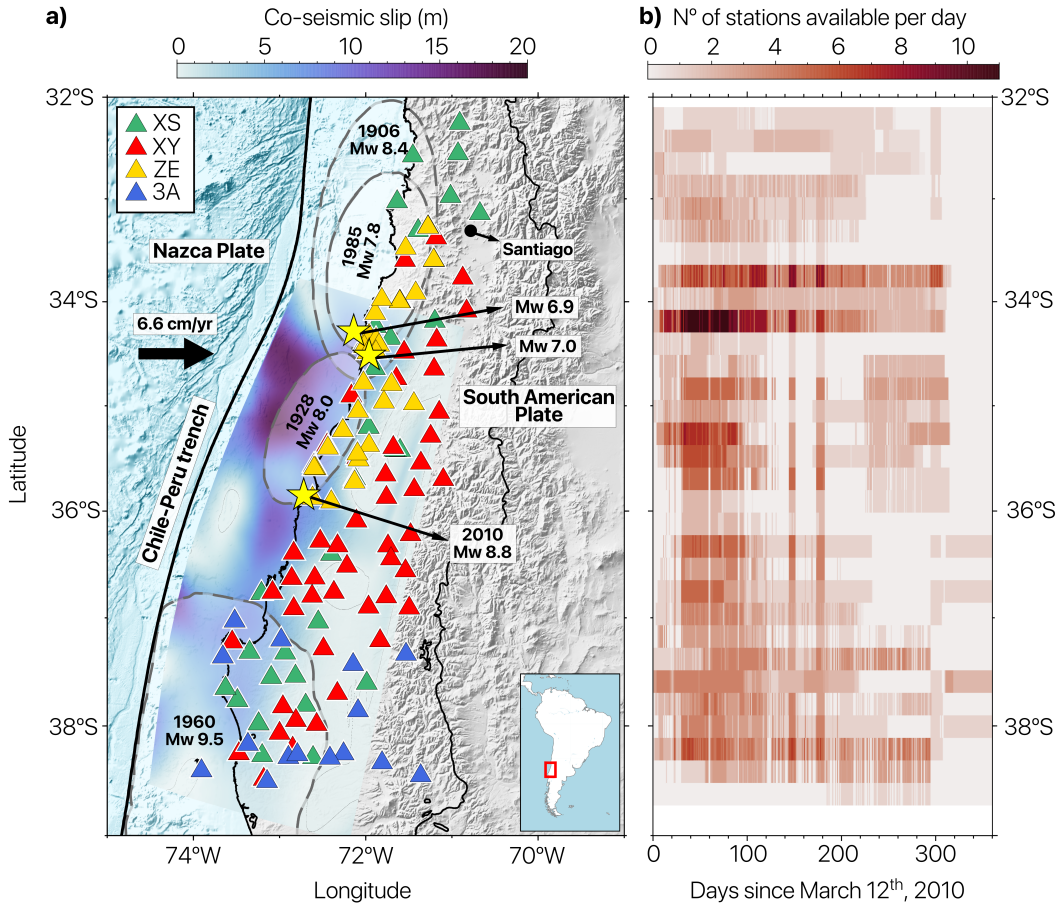


**Figure 1. Study area and data coverage.** (a) Seismic stations deployed in south-central Chile after the mainshock (triangles). Each color represents a network managed by different institutions: RESIF (XS in green, Vilotte et al., 2011), University of Florida (XY in red, Steve Roecker & Ray Russo, 2010), GFZ (ZE in yellow), and University of Liverpool (3A in blue, Beck et al., 2014). The coseismic slip model presented by (Yue et al., 2014) is represented in background colors, with darker zones related to larger slip. The yellow star marks the location of the  $M_w$  8.8 mainshock on February 27, 2010, as well as the largest aftershocks in the Pichilemu zone ( $34^{\circ}30'S$ ), with magnitudes  $M_w$  6.9 and  $M_w$  7.0, respectively. Historical rupture areas are depicted with gray ellipses. (b) Spatiotemporal availability of data. The color indicates the daily density of stations available every  $0.2^{\circ}$  of latitude.

uplift, and variations in mechanical coupling (Melnick et al., 2009). This geotectonically complex segment ruptured during the  $M_w$  8.8 mainshock and is believed to have released the strain accumulated since 1835 (Campos et al., 2002; Ruegg et al., 2009). The rupture nucleated near 36.5 S and propagated bilaterally, producing two major slip patches, a northern one with a peak up to 20 m, overlapping the probable 1928 rupture zone and extending north toward the 1985 rupture border, and a southern one, with approximately 10 m of slip overlapping the northern edge of the 1960  $M_w$  9.5 rupture zone (Figure 1a; Delouis et al., 2010; Lorito et al., 2011; Pollitz et al., 2011; S. Ruiz et al., 2012; Yue et al., 2014). Despite its magnitude, the Maule earthquake may not have fully released all the accumulated stress (Madariaga et al., 2010; Moreno et al., 2010), underscoring the role of margin segmentation and structural inheritance in governing rupture propagation and seismic potential. Along-strike changes in plate coupling, coseismic slip, and forearc structure suggest a segmented behavior of the Maule rupture, with contrasting conditions between the northern, central, and southern segments (Moreno et al., 2010; J. A. Ruiz et al., 2014; Tassara et al., 2016). The crustal Pichilemu fault system accommodates part of the shallow extension above the plate interface and hosts intense upper-crustal seismicity during the aftershock phase (Fariñas et al., 2011; Rietbrock et al., 2012). These contrasts in structure and kinematics provide a natural framework to interpret spatial variations in frequency–magnitude statistics and  $b$ -values, and to relate them to differences in coupling, stress conditions, and fluid content along the margin.

### 3 Data and Preprocessing

We retrieve one year of seismic data from the IMAD dataset, which corresponds to a postseismic mobile network operated by France, the United States, Germany, the United Kingdom, and collaborating partners, covering from March 2010 to March 2011 (see, e.g., Beck et al., 2014). This seismic array included nearly 156 instruments equipped with accelerometers, short-period seismometers, and broadband seismometers (Figure 1a). Stations were deployed across the entire rupture area (Figure 1a), though not all operated simultaneously or for the same durations (Figure 1b). Also, external conditions caused fluctuations in station availability over time, making the dataset less stable and uniform (Lange et al., 2012), so that at certain periods, fewer than 20 stations were operational, while at most, nearly 120 stations were simultaneously active.

To mitigate this variability, we exclude stations and traces with substantial data gaps. In regions with multiple stations within a 500 m radius, we select one station to avoid redundancy. Finally, we focus on periods with consistent availability of at least five stations, defined as the lowest threshold providing sufficient spatial and temporal coverage. This minimum threshold does not vary across the study area or over time, although the specific station combinations may change depending on the variable network configuration. The sequential steps of the workflow are illustrated in Figure 2, with further details provided in the subsequent sections.

We bandpass-filter the continuous data between 1 and 20 to discard low-frequency noise. We select this frequency range from an initial visual inspection of the data, which show energy concentrations mainly above 1 Hz. This approach is consistent with the parameters applied by Cabrera et al. (2021) in a similar tectonic context. Continuous waveforms were processed at the native sampling rates of each station, keeping them for the detection, relocation and magnitude estimation stages. In addition, we ensure the inclusion of only stations with minimal data gaps and consistent operational records. We include data segments if they meet two key criteria: (1) a minimum total duration of 75 % of the expected recording period for the event or station, ensuring sufficient temporal coverage despite potential gaps, and (2) individual contiguous chunks with a duration of at least 600 s, excluding excessively short fragments unsuitable for the analysis.

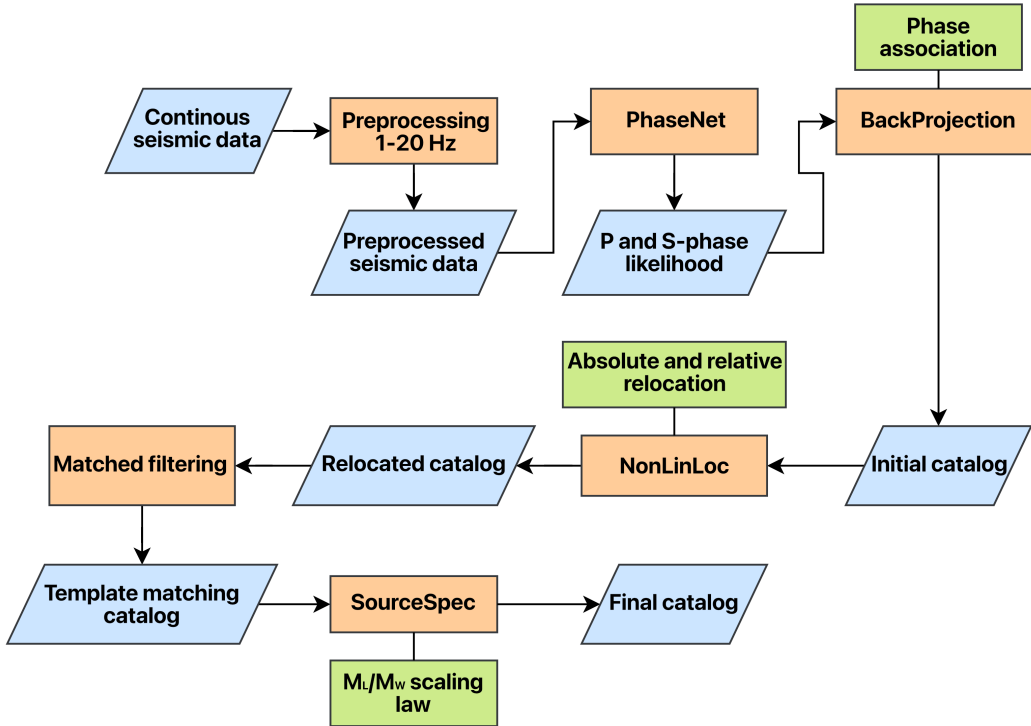


**Figure 2. Earthquake catalog workflow.** Blue boxes represent data (inputs or outputs), orange boxes indicate operations, and green boxes highlight some key steps. Continuous seismic data are filtered between 1 and 20 Hz and processed with PhaseNet to identify  $P$  and  $S$ -phase likelihoods. We associate the phases in space with backprojection to detect and locate the initial events, and relocate them with NonLinLoc. Additional techniques, such as template matching, contribute to increase the catalog completeness, while SourceSpec enables the magnitude estimation.

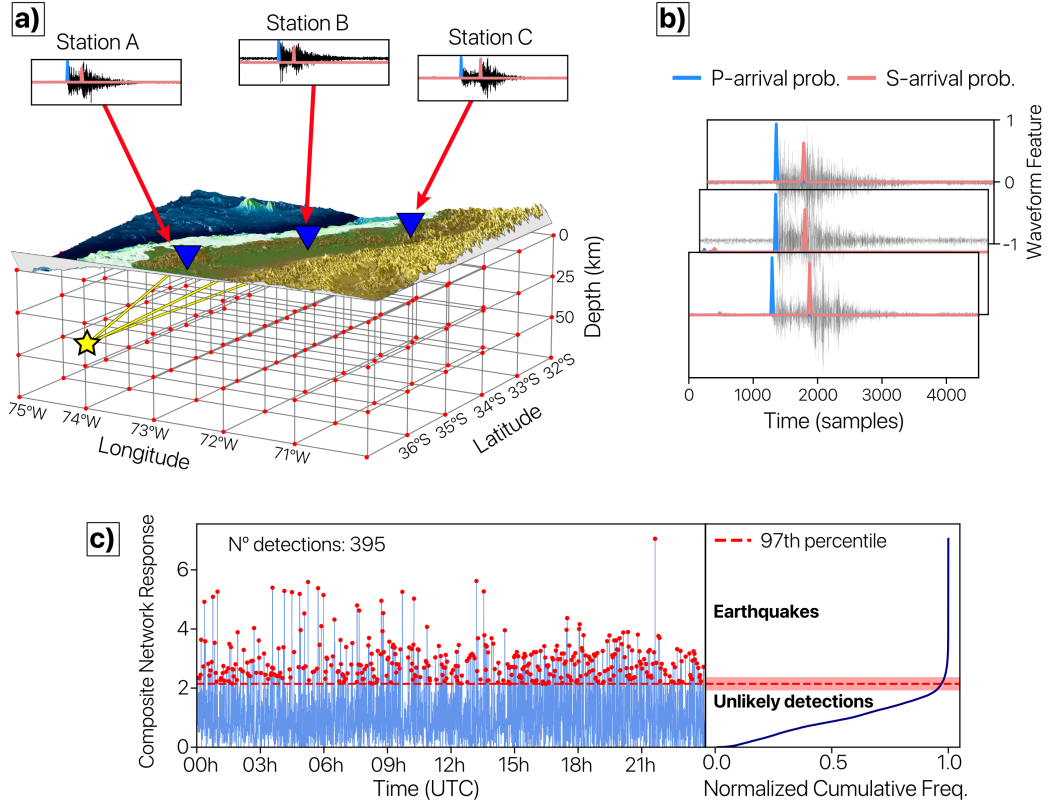


**Figure 3. Earthquake detection and initial location.** (a) Illustration of the grid with tested source points. The yellow star indicates the true earthquake location, with corresponding signals recorded at the seismic stations. (b) Example seismic record with the  $P$  and  $S$  likelihoods obtained using PhaseNet (Zhu & Beroza, 2019), shown in blue and orange, respectively. (c) Composite network response obtained by shifting and stacking the waveform features for each component and station over time (Beaucé et al., 2024). The detection threshold is indicated with a dashed red line, with red points indicating events interpreted as localized sources.

This workflow is based on the BPMF algorithm (Beaucé et al., 2024) whose outputs are post-processed with the NonLinLoc, Source-Specific Station Term (SSST) correction and waveform coherence relocation algorithm (Lomax & Savvaïdis, 2022) to enhance earthquake locations, and SourceSpec to estimate the moment magnitudes (Satriano, 2021). These tools complement the original framework and were included to increase the robustness of the results.

## 4 Earthquake Catalog

### 4.1 Detection and Phase Association

To detect and locate the initial earthquakes, we build a 3D spatial grid of potential point sources (Figure 3a). The grid covers the full extent of the rupture area, with a horizontal spacing of  $0.03^\circ$  in both latitude and longitude and a vertical spacing of  $0.5$ , reaching depths of up to  $100$ . This parameterization is consistent with the effective resolution of the 3D velocity model used in this study for south-central Chile (Figure S1 in the Support-

237 ing Information; Potin et al., 2025) and provides a practical compromise between spatial  
238 resolution and computational cost.

239 We compute the P- and S-wave travel times (moveouts)  $\tau_{sk}^\phi$  from each grid point  $k$  to  
240 station  $s$  for the seismic phase  $\phi \in \{P, S\}$  by solving the eikonal equation (White et al.,  
241 2020).

242 We then use the deep learning automatic phase picking algorithm PhaseNet (Zhu &  
243 Beroza, 2019) to estimate the probabilities  $\nu_{s\phi}(t)$  of  $P$ - and  $S$ -wave arrivals in continuous  
244 seismic data (as illustrated in Figure 3b and Figure S2 in Supporting Information). Next,  
245 we shift  $\nu_{s\phi}(t)$  according to the computed moveouts and stack the waveform features to  
246 identify the most likely source location. This serves as an efficient seismic phase association  
247 mechanism (see also Figure 3b). The stacked response, also named beamforming by Frank  
248 and Shapiro (2014), is defined as:

$$b_k(t) = \sum_{s \in \mathcal{S}_k} \sum_{\phi \in \{P, S\}} \nu_{s\phi} \left( t + \tau_{sk}^\phi \right). \quad (1)$$

249 Coherent seismic signals produce higher values of  $b_k(t)$  when aligned with a likely source  $k$ ,  
250 whereas incoherent noise does not contribute constructively. The set of seismic stations  $\mathcal{S}_k$   
251 only considers the ten closest stations to the source  $k$  to enhance source-to-station sensitivity.  
252 The final source location is determined by identifying the maximum value of the composite  
253 network response (CNR) defined as the beamforming maximum over time  $\mathcal{B}(t) = \max_k b_k(t)$ .

254 The CNR allows the detection and location of earthquakes with increased sensitivity  
255 and precision (Beaucé et al., 2019, 2022, 2024). It provides an initial estimate of the event  
256 location by identifying the time at which the beam power reaches its peak. However, the  
257 accuracy of this location strongly depends on the grid resolution and the velocity model. A  
258 finer grid, with more potential source points  $k$ , improves spatial precision but drastically in-  
259 creases computational cost. A key challenge in this process is to distinguish between beams  
260 corresponding to real earthquakes and those resulting from noise, unlikely signals, or arti-  
261 facts. Finally, given the large study area and the heterogeneous station coverage, the stacked  
262 signal response varies over time, making the choice of a detection threshold non-trivial. To  
263 address this, we implement a dynamic threshold approach based on the cumulative distri-  
264 bution function of the daily CNR. Assuming that most low-amplitude beams do not correspond  
265 to real events, we define the threshold at the inflection point, or “knee”, of the distribution  
266 (Figure 3c). However, in cases where the knee is not well-defined, the uncertainty in event  
267 detection could increase. To maintain a conservative yet effective detection criterion, we  
268 set the threshold at the 97<sup>th</sup> percentile of the beam power distribution. We also note that  
269 values between the 95<sup>th</sup> and 99<sup>th</sup> percentiles can effectively distinguish potential seismic sig-  
270 nals while reducing the likelihood of false detections. This adaptive approach ensures that  
271 the detection threshold dynamically adjusts to the empirical characteristics of the dataset,  
272 optimizing the balance between sensitivity and reliability.

273 Applying this approach, we detect 130,578 earthquakes during the study period. Each  
274 event has P- and S-wave picks from at least five stations, resulting in nearly six million  
275 valid picks (about 2.7 million P and 3.1 million S arrivals). Backprojection provides initial  
276 locations on the 3D grid described above, and the computations are accelerated on GPUs  
277 to keep runtimes practical for this large dataset.

## 278 4.2 Event relocation

279 To improve location accuracy, we relocate all detections with the NonLinLoc-SSST-  
280 Coherence algorithm (Lomax, 2001; Lomax et al., 2009; Lomax & Savvaïdis, 2022). Non-  
281 LinLoc uses the  $P$ - and  $S$ -wave picks previously identified by PhaseNet to perform a grid  
282 search and sample the likelihood of hypocenter locations in the regional 3D  $V_P/V_S$  velocity  
283 model (Figure S3 in the Supplementary Information; Potin et al., 2025). For each of the

130,578 events, it returns an absolute hypocenter and an uncertainty ellipsoid, which form the basis for the subsequent stages.

Then, we apply Source-Specific Station Term (SSST) corrections, which iteratively refine travel-time estimates by minimizing residuals between observed and predicted seismic phase arrivals (Figure S4). This approach accounts for spatial velocity variations, producing smoother station-specific travel-time corrections that adapt to regional heterogeneities, resulting in more precise earthquake locations. However, the S phase residuals show a consistently positive trend across stations (Figure S4), which suggests a systematic bias in the travel time predictions, likely caused by the network geometry. This mainly affects absolute depths and the most distant events, and it is partly mitigated by the coherence relocation, which sharpens relative locations within clusters.

Finally, we apply a relative relocation method based on waveform coherence (Lomax & Savvaïdis, 2022), conceptually similar to other techniques such as HypoDD (Waldhauser, 2001) or GrowClust (Trugman & Shearer, 2017), but without relying on differential travel times. High waveform coherence, quantified by the maximum cross-correlation, suggests that close events originate from nearby sources. We stack the location PDFs of highly correlated events and relocate them within their shared probability region. This approach enhances location accuracy, even in regions with sparse station coverage and limited datasets, such as in our case.

The result of this three-step workflow on the catalog is summarized in Figure 4. To allow a direct comparison of how earthquake locations evolve through the workflow, we plot only those events that successfully passed all relocation stages. Out of the initial 130,578 earthquakes, only one event retains its first location, 74,977 events are updated only by the SSST correction, and 55,600 events undergo the full coherence relocation. The median semi-major axis of the horizontal uncertainty ellipse is 1.2, the median semi-minor axis is 0.5, and the median vertical uncertainty is 1.6, for all the events. For the maps in Figure 4 we further restrict the plotting to the 49,230 relocated earthquakes with a horizontal uncertainty smaller than 10. In the outer rise zone (Figure 4a-c) the three panels look very similar, with only minor depth changes, which suggests that the offshore velocity structure and network geometry are still poorly constrained and vertical locations improve only slightly. In contrast, within the red box Figure 4a'-c', which encompasses the Pichilemu fault system, the relocation sharpens the seismicity distribution, with more compact clusters that better align with mapped structures.

### 4.3 Template matching

Template matching is a technique to identify new earthquakes with a low signal-to-noise ratio from existing templates (Anstey, 1964; Gibbons & Ringdal, 2006; Shelly et al., 2007; Frank & Shapiro, 2014; Skoumal et al., 2014; Beaucé et al., 2018; Cabrera et al., 2021; Beaucé et al., 2022; Minetto et al., 2022). This process quantifies the similarity between seismic waveforms, triggering a new detection when the correlation is sufficiently high (Figure S5). We define as templates a subset of earthquakes whose largest horizontal semi-major axis of the location error ellipse is smaller than 2. To avoid redundancy, we group highly correlated events and keep, for each group, the one with the smallest combined horizontal and vertical uncertainty. Each template consists of a 10 s window around the picked *P* wave on the vertical component and the picked *S* wave on the horizontal components.

We finally cross-correlate the continuous data with the templates in search of coherent signals. New detections are identified when the cross-correlation coefficient exceeds a time-dependent threshold, calculated as 8 times the Root Mean Square (RMS) of each 30 min segment, which is consistent with conservative thresholds used in previous template matching studies (e.g., Shelly et al., 2007; Ross et al., 2019; Beaucé et al., 2022). We require a minimum of three available stations and six channels to trigger a new detection, based on the network-averaged cross-correlation coefficient, and limit the search to a maximum

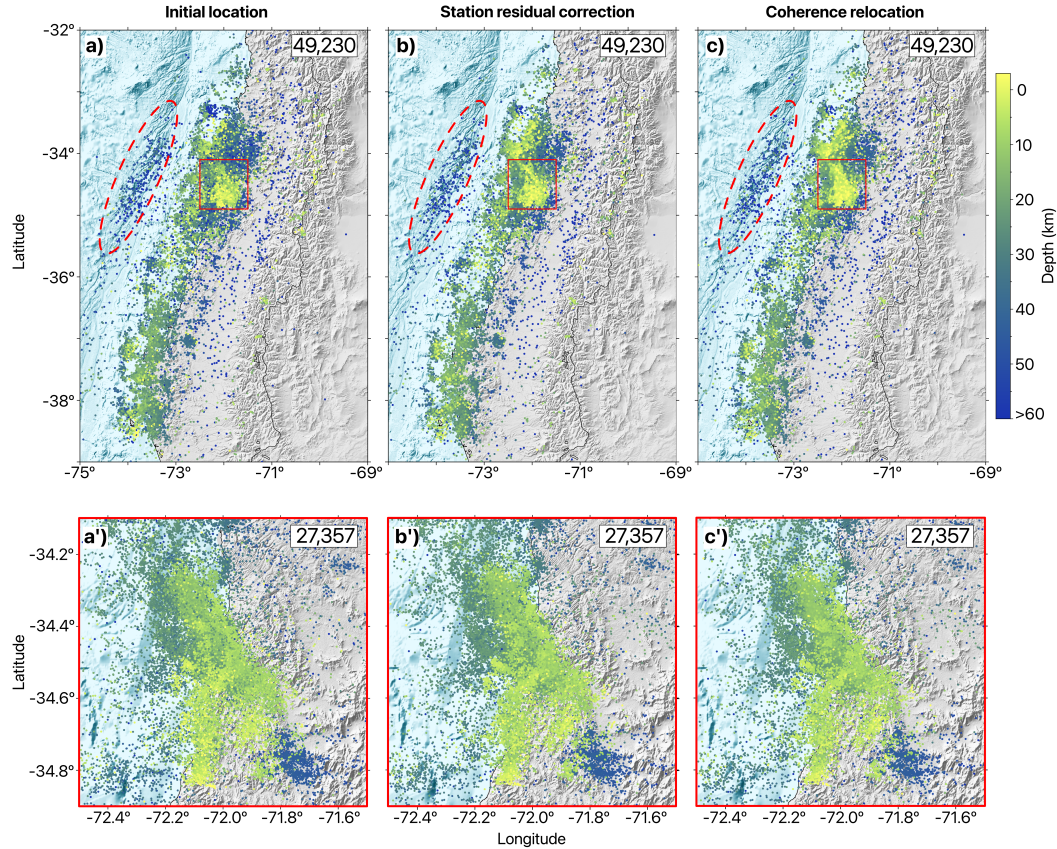


**Figure 4. Earthquake locations at different steps of the relocation process.** Panels (a–c) show the entire study area at different stages of relocation. The dashed red ellipsoid outlines the outer-rise zone, and the red box marks the area of the Pichilemu fault (a’–c’). (a–a’) Initial locations based on automatic picks by PhaseNet. (b–b’) Time residual corrections between observed picks and theoretical seismic phase arrivals, applied to the entire initial catalog. (c–c’) Relative relocation based on coherence of nearby seismic signals, which could only be applied to a subset of earthquakes, primarily those near the IMAD network. (a’–c’) Close-up view of the Pichilemu fault system, an area with a high concentration of aftershocks.

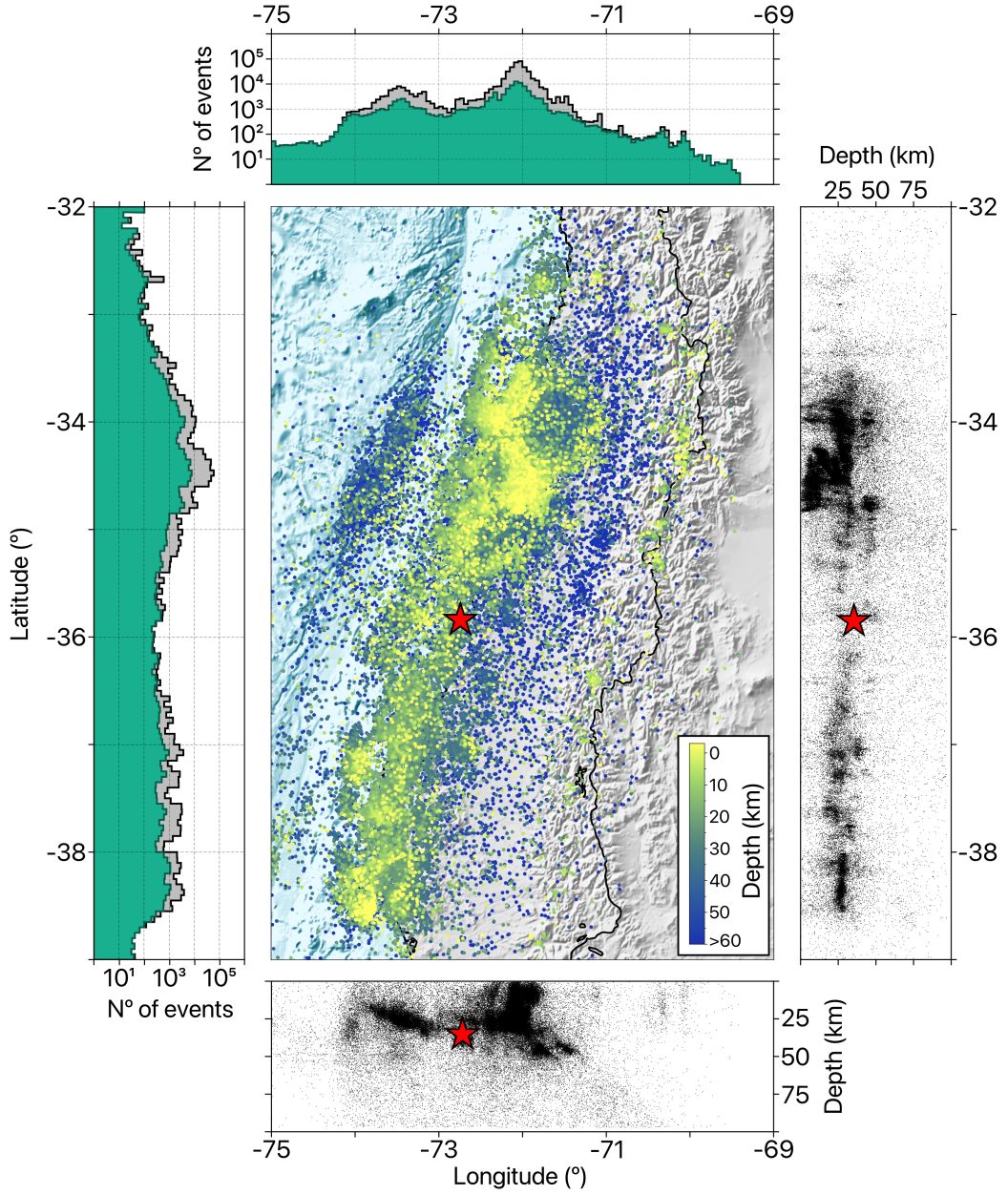


**Figure 5.** Spatial distribution of the aftershocks in the study area. The central panel corresponds to the final locations of the whole catalog, including the coordinates of the  $M_w 8.8$  mainshock, depicted with a red star and color coded by depth. The top and left panels respectively show the number of earthquakes as a function of longitude and latitude. The green histograms represent the initial catalog, while the grey histograms represent the final catalog after template matching. The right and bottom panels display stacked depth profiles of the earthquake catalog. The bottom panel clearly illustrates subduction across different longitudes, while the right panel shows the concentration of seismicity with latitude as a function of depth. The yellow star marks the location of the mainshock.

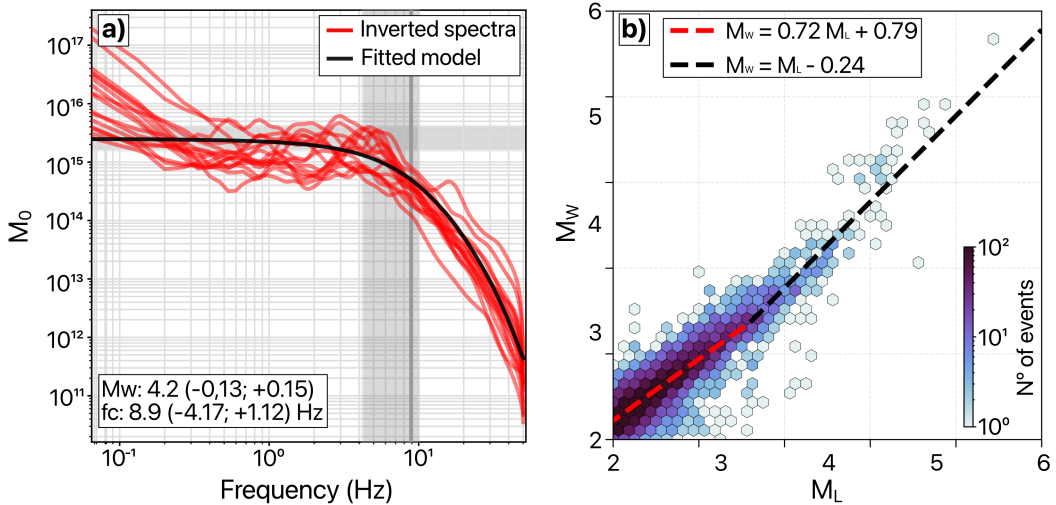


**Figure 6. Magnitude estimation method for the earthquake catalog.** (a) Seismic moment  $M_0$  plotted against the frequency content of the seismic signal for an example event. Red lines show the displacement spectra recorded at different stations for this event, with Brune's model fitted to the stacked spectra (black line). The vertical dark gray rectangle indicates the estimated corner frequency. (b) Local magnitude  $M_L$  calibration for moment magnitude  $M_w$  estimation for nearly 7,000 earthquakes in our catalog, represented by data with low standard deviation values.

of ten stations per template, selected based on proximity, to optimize performance in large seismic networks. For each new detection we assign the hypocenter of its parent template. Template detections therefore densify the catalog and extend the magnitude range, but they do not improve the spatial resolution beyond that of the template set. To ensure that the catalog contains only unique events, we apply a combination of geographic, temporal and similarity based filters. Events that occur within 4 s and 10 of each other are grouped as potential duplicates. Within each group we retain only one event, preferring the detection with the highest template correlation and, when correlations are similar, the one with the smallest location uncertainty. This procedure removes redundant detections while keeping the most reliable representative in each cluster.

From the relocation process, we identify 55,328 well-located earthquakes (with location uncertainties below 2 km) to serve as templates for template matching. To prevent redundant detections caused by highly similar events, we perform a waveform cross-correlation analysis, removing duplicates and retaining 37,990 unique templates. Applying template matching with these events results in the detection of 406,812 new earthquakes, increasing the number of events by a factor 10.7 compared to the starting subset of templates. We assign the locations of these newly detected events to their corresponding parent template, assuming that family members rupture closely spaced sources around the template hypocenter. As shown in the histograms in Figure 5 (top and left panels), the green area represents the initial catalog, while the gray area corresponds to the final catalog after template matching, with bin sizes of  $0.1^\circ$ . Most seismicity is concentrated in the Pichilemu area ( $34\text{--}35^\circ\text{S}$ ,  $71.5\text{--}72.5^\circ\text{W}$ ), where we identify the highest density of events both before and after template matching. In practice, the spatial resolution of the catalog is related to the 130,578 initial detected events and relocated with NonLinLoc–SSST–Coherence, while template detections mainly extend the temporal sampling and magnitude range along the same rupture area.

#### 361 4.4 Magnitude Estimation

362 To complete our earthquake catalog, we compute the moment magnitude ( $M_w$ ) using  
 363 the Hanks and Kanamori (1979) equation (see also Table S1 in Supporting Information):

$$364 M_w = \frac{2}{3}(\log_{10} M_0 - 9.1), \quad (2)$$

364 where  $M_0$  is the seismic moment, derived from the stacking and fitting of the Brune model  
 365 (Brune, 1970) to the  $S$ -wave displacement spectra recorded by the seismic network (Satriano,  
 366 2021). The obtained  $M_0$  values are then integrated into Equation 2 to compute  $M_w$ . Moment  
 367 magnitude is advantageous for representing earthquake size, as it does not suffer from  
 368 saturation and remains reliable across a broad range of seismic events. However, estimating  
 369  $M_w$  for small earthquakes is challenging because their related ground motion is often  
 370 masked by background noise. Accurate estimation of  $M_w$  for these minor events relies heavily  
 371 on the sensitivity of instruments and the density of near-field stations. For the smallest  
 372 earthquakes, the sampling rate also becomes a limiting factor, because their expected corner  
 373 frequencies approach or exceed the usable frequency band. In practice, we can only estimate  
 374  $M_0$  and  $M_w$  reliably for events whose spectra are well sampled around the corner frequency.

375 Therefore, for smaller events or when data quality is insufficient, we estimate  $M_w$  scaling  
 376 from local magnitudes ( $M_L$ ) to homogenize our catalog (Deichmann, 2017). To obtain  
 377  $M_L$  values for our earthquakes, we first recalibrate the distance-dependent attenuation term  
 378 in the classical Richter (1935) relation for south-central Chile. This calibration is performed  
 379 with a joint inversion of amplitude and distance, following the procedure and recommendations  
 380 of Bormann (2012) and similar regional studies (e.g., Langston et al., 1998; Y.-M. Wu  
 381 et al., 2005; Condori et al., 2017).

382 We use 7,119 events with reliable  $M_w$  values computed with SourceSpec (Satriano,  
 383 2021) as reference magnitudes. These earthquakes span from  $M_w \approx 2.0$  to 6.5 and cover  
 384 hypocentral distances between 10 and 250 km. The inversion includes a soft constraint that  
 385 keeps the estimated  $M_L$  close to  $M_w$  for events with small  $M_w$  uncertainties, so that the re-  
 386 sulting local-magnitude scale remains consistent with the moment-magnitude reference. For  
 387 each event–station pair, we extract the horizontal waveforms, simulate a Wood–Anderson  
 388 seismograph, and measure the zero-to-peak displacement amplitude, which we associate  
 389 with the corresponding reference  $M_w$  and hypocentral distance.

390 We describe the distance dependence with a two-term attenuation function that com-  
 391 bines geometric spreading and anelastic decay. For each event  $i$  and station  $j$  we assume

$$392 \log_{10} A_{ij} = M_{L,i} - a \log_{10} \left( \frac{R_{ij}}{R_{\text{ref}}} \right) - b (R_{ij} - R_{\text{ref}}) - S_j, \quad (3)$$

393 where each amplitude observation  $A_{ij}$  is related to the unknown local magnitude  $M_{L,i}$ , the  
 394 hypocentral distance  $R_{ij}$ , and a station correction  $S_j$ .

394 We solve for all parameters simultaneously using a least squares inversion. The coef-  
 395 ficients  $a$  and  $b$  control the average decay of amplitudes with distance, while  $S_j$  represents  
 396 a static correction that accounts for local site and instrument effects. To avoid trade-offs  
 397 between the  $S_j$  values and the overall magnitude level, we enforce that the network mean  
 398 of the station terms is zero, which defines a unique reference for the entire network.

399 We adopt a reference distance of  $R_{\text{ref}} = 100$  km, which is commonly used in regional  
 400  $M_L$  calibrations (Richter, 1935). This value also lies near the center of our sampled distance  
 401 range. The first term,  $a$ , mainly reflects the effective wavefront geometry and average crustal  
 402 structure, while the second term,  $b$ , represents moderate anelastic attenuation. The station  
 403 terms  $S_j$  describe local deviations from the mean amplitude field and are applied directly  
 404 in the final magnitude equation (Eq. 5) to correct for site-specific amplification.

405 This approach yields a stable and physically consistent calibration of the local magnitude scale, so we can compute homogeneous  $M_L$  values across the network and derive  
 406 consistent  $M_w$  estimates for smaller events.  
 407

408 The preferred solution of this inversion corresponds to,

$$409 \quad a = 1.4209, \quad b = 0.000736 \text{ km}^{-1}, \quad (4)$$

410 and provides a good fit to the amplitude data. The fit has a mean absolute error  
 411 of 0.19 magnitude units, a root mean square error of 0.25, and a negligible mean bias in  
 412  $\log_{10} A$  residuals. This root mean square error corresponds to a standard deviation of about  
 413 0.25 magnitude units in the residuals. At the event level, the anchored  $M_L$  values differ  
 414 from  $M_w^{\text{ref}}$  with a mean absolute difference of 0.20, a root mean square error of 0.30, and  
 415 a small positive bias of 0.09 in magnitude. These values indicate that the calibrated  $M_L$   
 416 scale is internally consistent with the observed amplitudes and externally consistent with the  
 417 reference  $M_w$ . Once the inversion parameters are fixed, we use the following  $M_L$  equation  
 in this study,

$$418 \quad M_L = \log_{10} A_{WA} + 1.4209 \log_{10} \left( \frac{R_{\text{hyp}}}{100} \right) + 0.000736 (R_{\text{hyp}} - 100) + S_j, \quad (5)$$

419 where  $A_{WA}$  is the Wood–Anderson zero to peak displacement amplitude and  $R_{\text{hyp}}$  is the  
 hypocentral distance in km.

420 Figure 6a illustrates the stacking of displacement spectra from multiple stations for an  
 421 earthquake (see also Figure S6 in Supporting Information), which we use to estimate the  
 422 seismic moment  $M_0$  and derive  $M_w$  (Equation 2). Based on this information, we calibrate the  
 423 local magnitude  $M_L$  to estimate  $M_w$  for the entire catalog using the following relationship:

$$424 \quad M_w = \begin{cases} 0.72M_L + 0.79 & \text{if } M_L \leq 3.6, \\ 425 \quad M_L - 0.24 & \text{otherwise.} \end{cases} \quad (6)$$

426 These two branches reflect the empirical observation that the scaling between  $M_L$  and  $M_w$   
 427 deviates from linearity at low magnitudes (Figure 6b). Following the approach presented  
 428 by Deichmann (2017), small earthquakes tend to follow a steeper scaling (approximately  
 429 1.5:1), while moderate to large events approach a 1:1 relationship. We apply a maximum  
 likelihood bilinear regression and identify a break point at  $M_L = 3.6$ , although the precise  
 break point may vary between datasets.

430 This approach homogenizes the catalog magnitude types and delivers  $M_w$  values ranging  
 431 from 0.22 to 6.20, with an average of 2.08 and a completeness magnitude  $M_c$  of around 1.8.  
 432 The majority of events cluster at lower magnitudes, with the first quartile at  $M_w$  1.83, the  
 433 median at  $M_w$  2.01, and the third quartile at  $M_w$  2.25. Approximately 90 of the events have  
 434 magnitudes below  $M_w$  2.61. Periodic spikes in event counts indicate intervals of increased  
 435 seismicity, which likely correspond to aftershock sequences. Most events fall within the  
 436  $M_w$  2–3 range, while the larger magnitudes, up to  $M_w$  6, are concentrated in the Pichilemu  
 437 region, which also hosted the two largest aftershocks ( $M_w$  7 and 6.9). However, the seismic  
 438 network became fully operational only a few days after these two events, so they are not  
 439 included in this catalog.

#### 440 4.5 Frequency–Magnitude Characteristics and $b$ -Value Estimation

441 We analyze the frequency and distribution of magnitudes across our study area, with  
 442 the widely applied linear logarithmic relationship (Gutenberg & Richter, 1944)

$$443 \quad \log_{10} N(\geq M) = a - bM, \quad (7)$$

444 where  $N(\geq M)$  represents the cumulative number of earthquakes with magnitudes greater  
 than or equal to  $M$ . The constant  $a$  estimates the seismic activity level in the region, while

445  $b$  indicates the relative proportion of high- to low-magnitude earthquakes, typically near  
 446 1. These parameters also serve to determine the catalog's magnitude of completeness  $M_c$   
 447 defined as the minimum magnitude at which the likelihood of detecting all earthquakes  
 448 approaches 1. However, this analysis may be biased in cases of periodically low availability  
 449 of stations or general incompleteness within the dataset (Geffers et al., 2022).

450 To address the challenges in estimating the  $b$ -value, we applied the  $b$ -more-incomplete  
 451 method (Lippiello & Petrillo, 2024), which builds upon the  $b$ -positive method (van der Elst,  
 452 2021) but improves accuracy by artificially increasing the level of incompleteness in the cat-  
 453 alog before estimating  $b$ . While the  $b$ -positive method calculates  $b$  from positive magnitude  
 454 differences between successive earthquakes, the  $b$ -more-incomplete method enhances robust-  
 455 ness by filtering out smaller events that could introduce bias due to partial detection. This  
 456 artificial filtering helps mitigate the effects of short-term aftershock incompleteness (STA1),  
 457 ensuring that the estimated  $b$ -value is less affected by time-dependent variations in detection  
 458 thresholds and minimizes the effects of overlapping coda waves and sparse network coverage  
 459 in the catalogs, resulting in a more accurate  $b$ -value estimation. In practice, the  $b$ -more-  
 460 incomplete progressively removes the smallest events until the estimated  $b$ -value becomes  
 461 insensitive to further changes in the magnitude threshold. This results in an effective  $b$  that  
 462 is controlled by the better recorded part of the catalog, without relying on the magnitude  
 463 of completeness.

464 The temporal variation in the number of available IMAD stations since March 12, 2010,  
 465 is shown in Figure 7a, together with the daily median location uncertainties of earthquakes.  
 466 Station availability fluctuates strongly, especially after the first three months, when a grad-  
 467 ual decline is observed, with only short week-long recoveries. Toward the end of the period,  
 468 the number of available stations stabilizes at approximately 15. These fluctuations directly  
 469 affect earthquake detection and location accuracy, and periods of reduced station coverage  
 470 coincide with increased location uncertainties (Figure 7a). This effect is also evident in  
 471 Figure 7b, where regions with dense station coverage (Figure 1b), such as Pichilemu (34  
 472 to 35 S), exhibit a higher density of events. Conversely, regions with lower station avail-  
 473 ability show detection gaps, particularly between 35 to 37 S after about 100 days from the  
 474 start of the study period. Larger magnitude events are predominantly concentrated at the  
 475 beginning of the sequence and are mostly related to the Pichilemu area, which further en-  
 476 hances the contrast in detection rates between space and time. As shown in Figure 7c, the  
 477 magnitude distribution over time highlights a strong concentration of events around  $M_w$   
 478 2. The earthquake detection rates (Figure 7c) display the expected decay over time, with  
 479 occasional swarms that coincide with short-term increases in station availability and local  
 480 network reactivation. This underlines the strong impact of station coverage on the inter-  
 481 pretation of earthquake catalogs. It also highlights the importance of having well located  
 482 events, since there are periods where template matching could not be applied because of  
 483 the lack of reliable reference locations, which produces a heterogeneous spatial distribution  
 484 of new template detections.

485 We compute the  $b$ -value using two different methods, as illustrated in Figure 7d. For  
 486 this analysis, we use batches of 5,000 earthquakes to estimate the  $b$ -value as a function of  
 487 time. Tests with 3,000 and 7,000 event windows give similar long-term trends, and 5,000  
 488 events offer a good compromise between temporal resolution and stability. The black line  
 489 represents the  $b$ -values obtained with the classical maximum likelihood method for events  
 490 above  $M_c$ , while the red line corresponds to estimates from the  $b$ -more-incomplete method  
 491 (Lippiello & Petrillo, 2024). At the beginning of the sequence, the classical  $b$ -values fluctuate  
 492 between about 0.6 and 1.2, then they show a spike up to about 1.6 around day 120, and  
 493 later fluctuate around 1.2 before tending toward a stable value close to 1.0 at the end of the  
 494 period. The early values are characteristically low for an aftershock sequence, which likely  
 495 reflects the limited station coverage and the resulting loss of small events in the catalog.  
 496 In contrast, the  $b$ -more-incomplete estimates show a much more stable behavior over time,

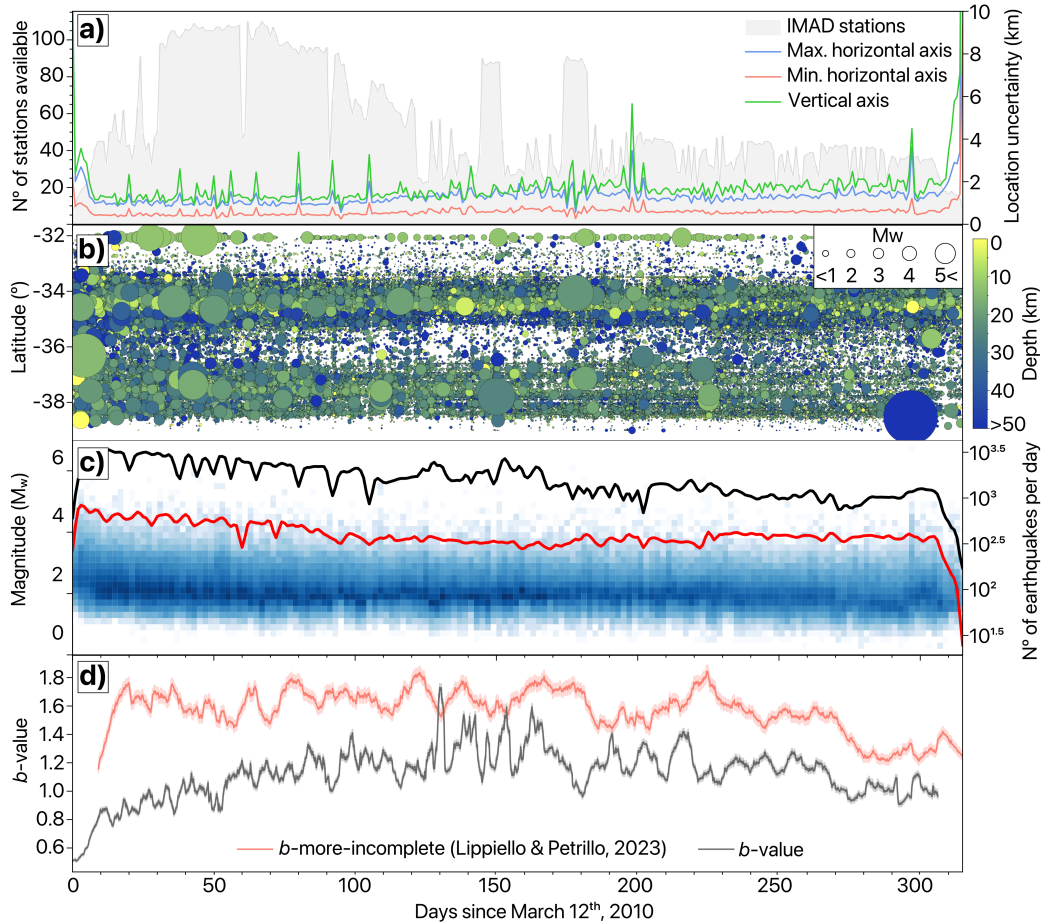


**Figure 7.** Temporal variations in (a) station availability (gray area) and earthquake location uncertainties (colored lines for maximum axis, minimum axis, and depth), (b) the spatial distribution in latitude, where circle size represents event magnitude and color indicates depth, (c) the magnitude variation in the final catalog (blue squares), and the trends accounting for the number of earthquake detected per day, from the initial catalog (red) and the final catalog (black), and (d) the estimated  $b$ -value using the  $b$ -more-incomplete method. Shaded areas indicate the uncertainty ranges for both methods. The  $b$ -more-incomplete method is less sensitive to time-dependent changes in detectability than the classical maximum likelihood estimator.

497 with values that remain mostly between 1.2 and 1.6 during the first part of the sequence  
 498 and then converge toward a value close to 1.0 near the end.

499 Values of  $b$  above 1 indicate a relative predominance of smaller earthquakes over larger  
 500 ones, which is typical for aftershock sequences. The fact that the  $b$ -more-incomplete method  
 501 can be applied to more incomplete catalogs and relies on magnitude increments rather than  
 502 strict completeness makes it less sensitive to station-dependent variations in detectability.  
 503 As a result, it provides a more robust description of the temporal evolution of  $b$  in this  
 504 sequence and reduces the impact of changes in station availability on the inferred stress  
 505 state.

## 506 5 Discussion

### 507 5.1 Workflow Performance and Limitations

508 In this study, we employ the BPMF automated detection and location workflow (Beaucé  
 509 et al., 2024) to build a dense and internally consistent catalog of the Maule aftershock se-  
 510 quence. The workflow performs well across most of the study area, although its effectiveness  
 511 still depends on the daily station coverage, which remains the main limitation of the Maule  
 512 network. PhaseNet produced between 6,000 and 12,000 P picks per day on average (maxi-  
 513 mum around 24,000), and a similar number of S picks, even though the number of available  
 514 stations changed strongly over time. Nevertheless, the performance decreases for distant  
 515 offshore events where S-P times exceed 30 s. The sparse and time-variable network further  
 516 limits detection consistency, especially during periods of strong data gaps.

517 Within the BPMF workflow, detections rely on the coherence of PhaseNet P and S  
 518 probability time series across stations rather than on the performance of individual sen-  
 519 sors. A real earthquake produces coherent probability increases at consistent moveouts, so  
 520 even low probabilities sum constructively and generate a clear CNR peak. This makes the  
 521 detector sensitive to low amplitude events without requiring station-specific thresholds.

522 Because the Maule network is sparse and highly variable in time, the amplitude of the  
 523 CNR fluctuates strongly across days. In such conditions, a fixed detection threshold, as  
 524 used in more stable networks (Beaucé et al., 2019, 2022), would either miss many events on  
 525 quiet days or admit too many false detections when noise levels are high. Instead, we use a  
 526 day-dependent threshold based on a high percentile of the daily CNR distribution, typically  
 527 the 97th percentile (see Section 4.1). This percentile-based threshold keeps the detection  
 528 performance more homogeneous through the 10-month sequence, at the cost of losing the  
 529 smallest events on the quietest or noisiest days.

530 Location accuracy benefits from the regional 3D velocity model (Potin et al., 2025),  
 531 which improves the coherence of clusters in the central and northern parts of the domain,  
 532 including the Pichilemu region. The improvement is clear in map view and in cross sections  
 533 (Figure 10 and Figure S7 in the Supporting Information), where previously diffuse clouds  
 534 align into narrower structures. However, certain areas remain less well constrained. Offshore  
 535 events in the outer rise zone and events south of 37 S are affected by reduced station coverage  
 536 and lower resolution in the velocity model. These locations should be interpreted with  
 537 caution. Overall, the workflow performs well for a sparse and heterogeneous network, but  
 538 it does not replace the benefits of a dense permanent array.

539 The matched filter search is stable in this region. Some station-template correlations  
 540 can be low (0.2–0.3), but averaging across at least five stations and six channels and applying  
 541 a median absolute deviation criterion yields robust detections even when individual traces  
 542 are noisy. This strategy is widely used in BPMF applications (Beaucé et al., 2019, 2022,  
 543 2024) and behaves similarly in the Maule dataset. Matched filtering densifies the catalog  
 544 and lowers the magnitude of completeness, but newly detected events inherit the location  
 545 of their template. These detections refine the temporal sampling and magnitude range of

546 the sequence rather than its spatial resolution. The GPU implementation of BPMF makes  
 547 the backprojection and template matching stages fast and scalable.

548 Our regional  $M_L$  calibration reproduces the reference magnitudes with small bias but  
 549 still leaves some residual variability. The residuals, shown in Figure S8 in Supporting  
 550 Information, defined as  $M_{\text{ref}} - M_{\text{pred}}$  for each event, are centered near zero and most values  
 551 lie between about  $-0.5$  and  $0.5$  magnitude units over distances from  $10$  to  $250$  km, with  
 552 only a few outliers reaching larger absolute values. There is no strong systematic drift with  
 553 distance, although a mild trend remains at the smallest magnitudes. This suggests that the  
 554 calibration captures the main attenuation pattern and that the remaining scatter is domi-  
 555 nated by unresolved path and site effects, together with measurement noise. When residuals  
 556 are averaged over several stations per event, they translate into typical  $M_L$  uncertainties of  
 557 about  $0.2$ – $0.3$  magnitude units. A more detailed study of frequency-dependent  $Q$ ,  $\kappa$ , and  
 558 site amplification, using a generalized inversion technique (GIT) to separate source, path,  
 559 and site contributions on the same dataset, could further reduce this scatter, but this is  
 560 beyond the scope of the present work. Despite this scatter, the calibrated  $M_L$  scale is inter-  
 561 nationally consistent and stabilizes the  $M_w$ – $M_L$  relation in the magnitude range most relevant  
 562 for our aftershock statistics. This internal coherence is what matters for estimating  $b$ -values,  
 563 mapping spatial variations in seismicity, and comparing the behavior of the crust and the  
 564 subducting slab.

## 565 5.2 Comparison with Previous Catalogs

566 This aftershock sequence has already been the focus of previous studies, resulting in  
 567 the development of other earthquake catalogs. For instance, Lange et al. (2012) utilized  
 568 automatic picking methods to compile a catalog of over 20,000 events spanning the first six  
 569 months of the sequence. Similarly, Rietbrock et al. (2012) applied the STA/LTA triggering  
 570 method with 2D velocity models, detecting and locating approximately 40,000 earthquakes.  
 571 While most of their detailed analyses focus on roughly the first two months after the main-  
 572 shock, the published catalog spans nearly 300 days of seismicity. Additionally, Ryder et al.  
 573 (2012) produced a catalog using comparable methods, although limited to a shorter period  
 574 of two and a half months. All these works provided the foundation for our current under-  
 575 standing of the Maule aftershock sequence and were produced with the methods available at  
 576 the time. They all rely on the same mobile seismic network (IMAD) used in this study. We  
 577 revisit the same dataset using modern detection and relocation techniques, with the goal  
 578 of extending the magnitude range, improving location accuracy, and resolving smaller scale  
 579 structures within the Maule rupture zone.

580 These catalogs have served as the basis for numerous subsequent studies, including the  
 581 characterization of afterslip seismic patterns (Agurto et al., 2012) and the development of  
 582 velocity models through local earthquake tomography, which have revealed new structural  
 583 features in this segment of the subduction zone (Hicks et al., 2014). Major structures  
 584 associated with the Maule earthquake rupture, such as those linked to the subduction slab  
 585 and the crustal portion with high seismic activity near Pichilemu, are well represented in  
 586 these catalogs (e.g., Ryder et al., 2012) and are consistent in the seismicity distribution.  
 587 However, the resolution of fine-scale seismic structures has remained limited.

588 Figure 8 compares the magnitude distribution, temporal evolution, and spatial coverage  
 589 of seismicity in three catalogs: Rietbrock et al. (2012), the International Seismic Catalog  
 590 (ISC) (Di Giacomo et al., 2018), and ours, for the same time period. While all catalogs  
 591 achieve consistent detection completeness for  $M_L \geq 3$ , our catalog captures a significantly  
 592 higher number of small-magnitude events ( $M_L \leq 2$ ). This improvement is especially clear  
 593 during periods of low station coverage, where the adaptive threshold and matched-filter  
 594 detections maintain stable performance. Our workflow detects 130,578 initial earthquakes  
 595 and 537,390 total events after template matching, compared with 40,087 events in the catalog  
 596 of Rietbrock et al. (2012) and 5,261 events in the ISC catalog (Di Giacomo et al., 2018).

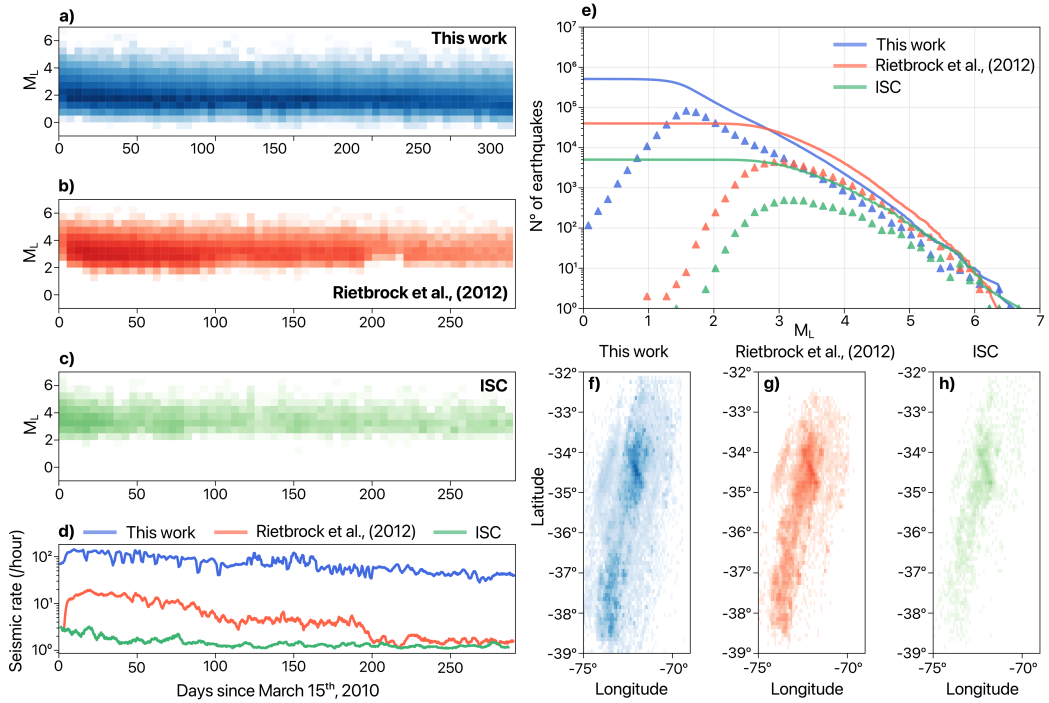


**Figure 8.** Comparison of three earthquake catalogs based on magnitude distribution, temporal evolution, and spatial coverage for the same period. (a), (b), and (c): 2D histograms showing the distribution of local magnitudes ( $M_L$ ) over time with bins of 5 days and 0.5 in magnitude. Blue represents the catalog presented in this study, red corresponds to the catalog by Rietbrock et al. (2012), and green denotes the catalog from the ISC (Di Giacomo et al., 2018). Lighter tones indicate lower data density, while darker tones represent higher densities. (d): Seismicity rate (events per hour) over time for the three catalogs, following the same color coding. (e): Magnitude-frequency distribution for the three catalogs. Solid lines represent the cumulative number of events following the Gutenberg–Richter law, while triangles indicate the number of earthquakes for each magnitude bin. (f), (g), and (h): Spatial distribution of seismicity in the rupture zone for each catalog.

597 This increase reflects the combined effect of improved phase picking and matched filtering.  
 598 The magnitude of completeness also improves from  $M_c \approx 2.7$  in Rietbrock et al. (2012) and  
 599 above 3.5 in ISC to  $M_c \approx 1.8$  in our catalog, which corresponds roughly to a 10-times gain  
 600 in sensitivity.

601 The seismicity rate, as shown in Figure 8d, shows similar temporal trends across the  
 602 three catalogs, but with clear differences in the total number of recorded events. In all three  
 603 catalogs, short-term drops in rate follow larger earthquakes, when coda waves mask smaller  
 604 aftershocks. These systematic gaps underscore the need to account for detection limits when  
 605 interpreting aftershock productivity.

606 The frequency–magnitude distribution of our catalog, compared to the catalogs of  
 607 Rietbrock et al. (2012) and the ISC, is presented in Figure 8e. This comparison high-  
 608 lights the improved detection capability of the proposed workflow, which achieves a lower  
 609 magnitude of completeness by 1 to 2 orders of magnitude, significantly expanding the range  
 610 of detectable seismic events. Differences in the number of moderate-magnitude events also  
 611 reflect the fact that each catalog relies on a distinct local–magnitude scale. The Rietbrock  
 612 et al. (2012) catalog uses a different  $M_L$  formulation based on the methods available at  
 613 the time, while our study recalibrates a regional attenuation model directly from the Maule  
 614 dataset. Because the ISC catalog relies on a low-density permanent network, it detects fewer  
 615 events across all magnitude ranges.

616 Figure 8f–h show that the overall shape of the seismicity distribution is consistent be-  
 617 tween catalogs, with a pronounced concentration around the Pichilemu region. Overall, our  
 618 catalog reveals additional small-scale structures and secondary clusters, particularly in the  
 619 Pichilemu fault area and in the central part of the rupture. In Pichilemu, aftershocks cluster  
 620 more tightly along narrow NNW-striking structures and secondary NE-trending branches  
 621 than in previous Maule catalogs. In Figure S7, we compare our locations with those of  
 622 Rietbrock et al. (2012) using identical map views and cross sections. The tighter clusters  
 623 and improved spatial coherence highlight the gains from combining increased completeness  
 624 with a 3D velocity model and successive relocation stages (see Text S1 and Figure S7 in  
 625 the Supporting Information). This improved resolution, together with the regional  $M_L$  cal-  
 626 ibration, allows us to map spatial and temporal  $b$ -value variations that were not resolved in  
 627 earlier work. These improvements are most robust in regions with dense station coverage  
 628 and good velocity control, whereas offshore and southern areas remain less well constrained  
 629 and should be interpreted carefully.

630 We successfully re-detect approximately 88 % of the events reported by Rietbrock et al.  
 631 (2012) and 90 % of those cataloged by the Centro Nacional de Sismología de Chile (CSN)  
 632 and the ISC (Di Giacomo et al., 2018). Events not recovered usually correspond to signals  
 633 with too few picks to meet the internal consistency criteria of our workflow. Excluding them  
 634 keeps the catalog homogeneous and avoids introducing poorly constrained detections.

### 635 5.3 Geotectonic Implications

636 This catalog provides a detailed and consistent view of the aftershock sequence of the  
 637 2010 Maule earthquake and shows how different structural domains responded to the main-  
 638 shock. The most intense postseismic activity occurs in the Pichilemu area (Figure 9, B-B'  
 639 and Figure 10), where a shallow normal fault system accommodates upper crustal extension  
 640 above the main slip patch. The normal-faulting nature of this system and its potential  
 641 reactivation within the area of highest coseismic slip have been already well documented  
 642 (Farías et al., 2011; Lange et al., 2012; Ryder et al., 2012; Lieser et al., 2014). Using  
 643 the increased number of small earthquakes, we refine the view of the Pichilemu fault sys-  
 644 tem in Figure 10. Seismicity related to this fault system was isolated using HDBSCAN,  
 645 a hierarchical density-based algorithm (Campello et al., 2013), often used to distinguish  
 646 earthquake patterns within catalogs (Essing & Poli, 2024). The clustering was applied in  
 647 four dimensions considering location coordinates and origin time.

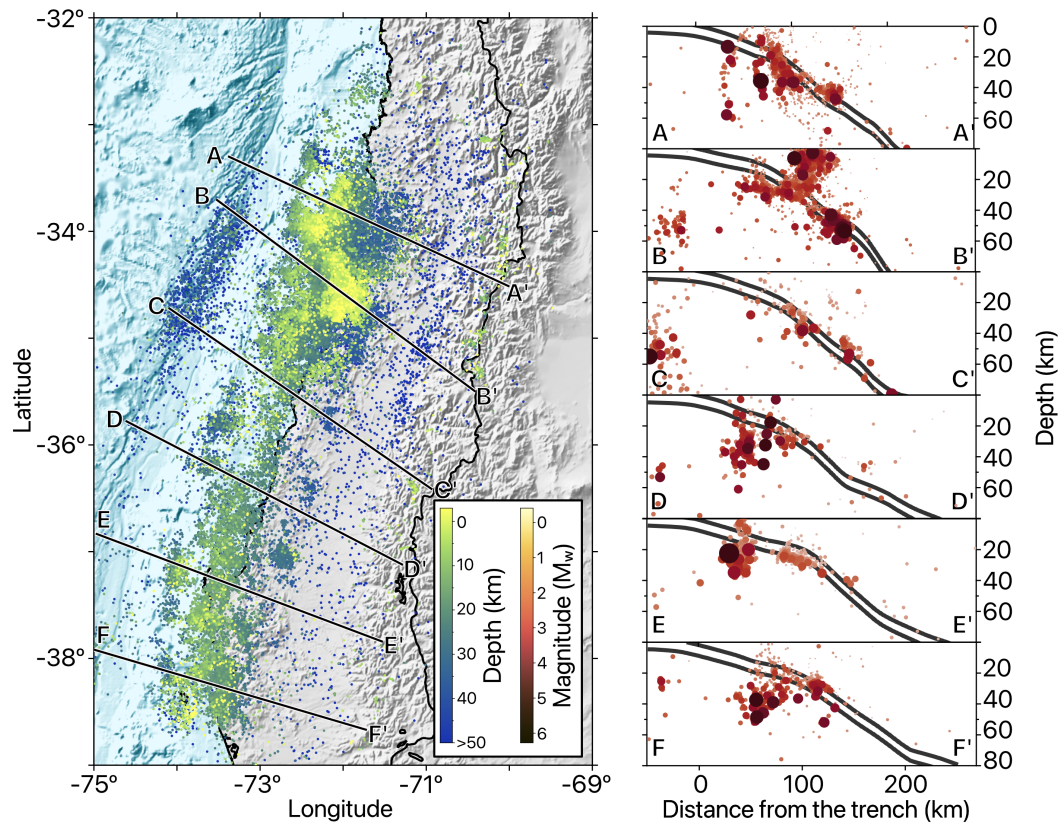


**Figure 9.** Spatial distribution of seismicity (colored dots) and profiles perpendicular to the subduction trench (black lines, A-F). On the left panel, color represents depth, while in the cross-sections on the right (A-F), color indicates magnitude. Black lines in the cross-sections correspond to the slab model (Slab 2.0, Hayes et al., 2018) for the subduction zone in this region.

648 In this area, we observe a main normal fault characterized by an azimuth–dip orientation  
 649 of N40 W/S30 W and extending for about 49 (Figure 10, A–A'). The fault system shows  
 650 distinct seismic patterns, with branches approximately perpendicular to the main structure  
 651 and forming an L-shaped distribution. Seismicity is concentrated between 5 and 20 depth  
 652 along these intersecting faults, defining a seismogenic thickness of roughly 5 km and a  
 653 distributed deformation field around the main fault.

654 This configuration points to a conjugate normal-fault system, where secondary NE–SW  
 655 structures intersect the main NW–SE fault. The geometry is typical of upper-plate exten-  
 656 sional regimes along the Chilean margin (e.g., J. A. Ruiz et al., 2014; Piquer et al., 2019;  
 657 Santibáñez et al., 2019) and is consistent with seismological models of the largest 2010  $M_w$   
 658 7.0– $M_w$  6.9 aftershocks in the area (J. A. Ruiz et al., 2014). Comparable conjugate fault  
 659 patterns have been described in other complex normal-faulting sequences, such as the  $M_w$   
 660 6.5 Ludian earthquake (Li et al., 2024) and the  $M_w$  7.1 Ridgecrest earthquake (Liu et al.,  
 661 2019), supporting an interpretation in terms of localized crustal stretching and stress trans-  
 662 fer within the upper plate. Altogether, the seismicity distribution offers a coherent and  
 663 high-resolution seismological image of the Pichilemu fault system and provides new con-  
 664 straints on its geometry and on the mechanisms of upper-plate fault reactivation in central  
 665 Chile.

666 Offshore Pichilemu, we also observe clear seismic activity in the outer-rise zone. This  
 667 finding aligns with previous studies, which suggest that this seismicity is a direct response  
 668 to the high coseismic slip in the region, potentially resulting from the activation of shal-  
 669 low normal fault systems under extensional forces following large slip events (Moscoso &  
 670 Contreras-Reyes, 2012; Lange et al., 2012; Rietbrock et al., 2012; J. A. Ruiz & Contreras-  
 671 Reyes, 2015). Several events appear near or below 30 depth. These values should be  
 672 interpreted with caution because long travel paths and possible mixing between direct and  
 673 reflected phases can affect depth estimates in this offshore region.

674 Seismic activity associated with the subducting slab is present throughout the rupture  
 675 zone. Notably, two distinct bands of seismicity are observed along the profiles: one at  
 676 depths of 20 km to 35 km (Figure 9, A–F) and another, deeper band at approximately  
 677 50 km, primarily in Figure 9, A–C. A horizontal gap in seismicity is evident in the region  
 678 closest to the mainshock (Figure 5), suggesting minimal post-mainshock activity in this  
 679 area, likely due to significant coseismic stress release. While some seismicity does not align  
 680 precisely with the slab model, it follows a consistent depth distribution, highlighting distinct  
 681 tectonic behaviors captured by this catalog.

682 A marked decrease in aftershock activity is observed around 36°S, near the mainshock  
 683 hypocenter, forming a distinct low-seismicity zone within the rupture area (Figures 9 and  
 684 5). South of this region, toward Concepción, the sequence shows sparse and discontinuous  
 685 seismicity, with small clusters separated by aseismic patches (Figure 9). This quiescence  
 686 is consistent with substantial coseismic stress release and a limited postseismic response in  
 687 the southern segment. The scarcity of shallow or interface events emphasizes the along-  
 688 strike segmentation of deformation and the heterogeneous reactivation of the plate interface  
 689 following the Maule earthquake. Overall, these patterns outline how the crustal faulting  
 690 system, the outer-rise region, and the slab responded to stress redistribution after the Maule  
 691 earthquake.

#### 692 5.4 Spatial Patterns of Seismicity and $b$ -Value Variations

693 The  $b$ -value provides a simple way to follow how stress and structure vary across the  
 694 rupture zone, being linked to fault coupling, stress regime, and fluid content (Custódio  
 695 & Archuleta, 2006; Chiba, 2019; Folesky, 2024; Collettini & Tinti, 2025). We estimate it  
 696 using two approaches, the classical maximum likelihood method (Aki, 1965) and the  $b$ -more-  
 697 incomplete method (Lippiello & Petrillo, 2024), which reduces the impact of time-variable  
 698 completeness. The classical estimate starts with unusually low values (0.6–1.2) during the

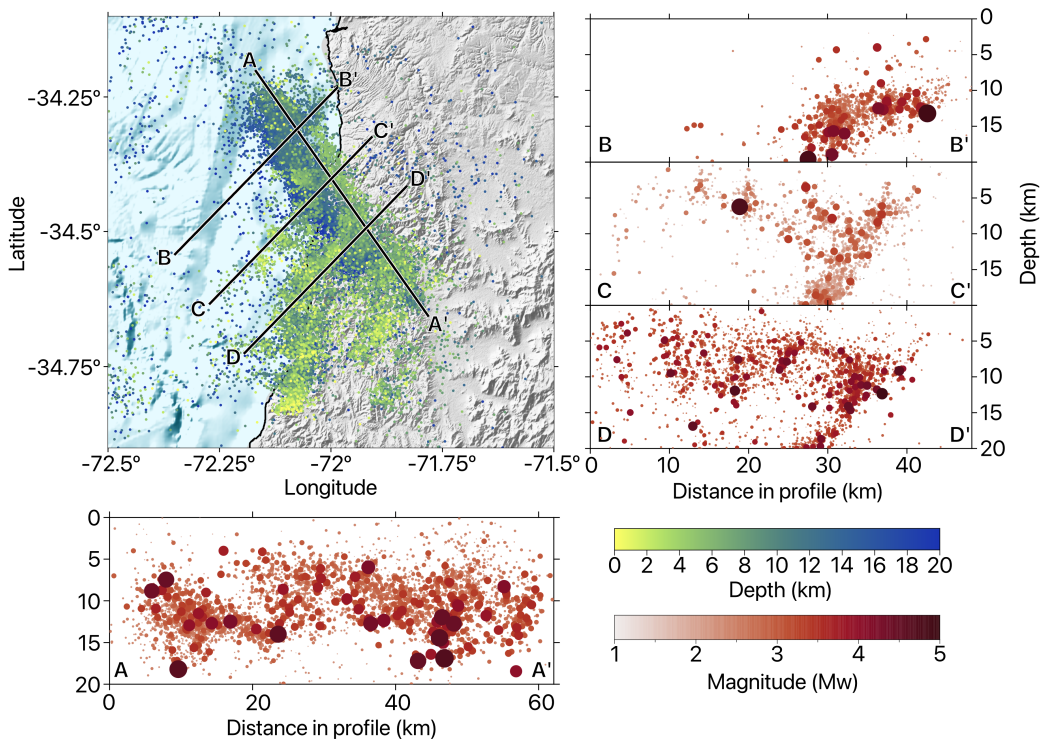


**Figure 10. Spatial evolution of the Pichilemu fault system.** Earthquakes are shown as dots color-coded by depth in the latitude-longitude map, and by the estimated moment magnitude ( $M_w$ ) in the cross-sections. Profiles along the black lines (A-D) include one in the main Pichilemu fault's azimuthal direction (A-A') and three perpendicular sections (B-D). The cross-sections illustrate the southwest dip direction of the northwest-trending fault and a series of conjugate faults, forming an L-shaped faulting system.

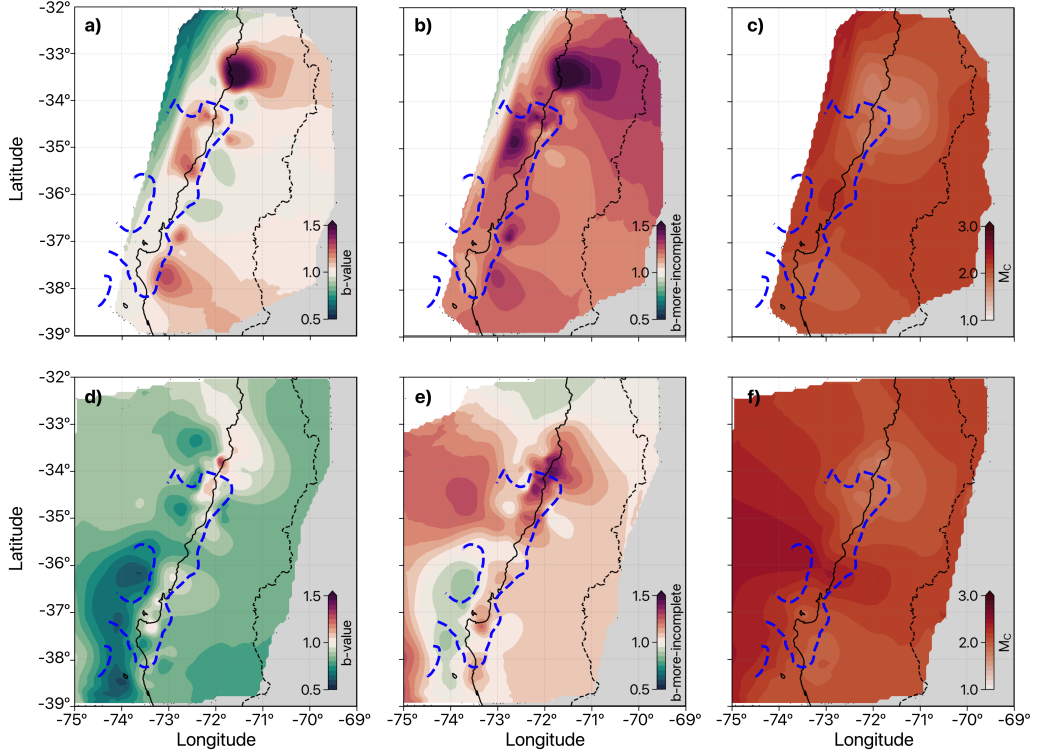


**Figure 11. Spatial distribution of the  $b$ -value and  $M_c$ .** We compute these values within earthquake clusters of at least 200 events. (a–c) Crustal seismicity. (d–f) Slab-related seismicity. Columns show the classical  $b$ -value, the  $b$ -more-incomplete estimate, and the corresponding  $M_c$ . The dashed blue line marks the 5 m coseismic slip contour from the model of Yue et al. (2014); regions inside the contour correspond to slip values exceeding 5 m.

first weeks, rises sharply to  $\sim 1.6$  around day 120, and then stabilizes near 1.0 toward the end of the period (Figure 7d). In contrast, the  $b$ -more-incomplete remains much more stable, mostly between 1.2 and 1.6 during the first months, and gradually converges toward a value close to 1.0. These differences are closely linked to the evolution of station availability. As shown in Figure 7a, the number of IMAD stations decreases from more than 80 at the start to about 15 at the end of the study period, which affects detectability. As a result, the classical method drops to 0.6–0.8, while the  $b$ -more-incomplete remains stable at 1.2–1.6, as it is less sensitive to short-term aftershock incompleteness and variable detection thresholds.

To map spatial variations (Figure 11), we follow an iterative clustering strategy (Hartigan, 1975). For each of the  $N = 100$  iterations, we randomly select a number of clusters  $k$  between 50 and 500 and obtain them using mini-batch k-means (Sculley, 2010; J. Wu, 2012). This produces clusters of variable size, with a typical target of about 400 events per cluster. Clusters with fewer than 200 events are discarded to ensure stable statistics. For every iteration, we estimate  $M_c$ , the classical  $b$ -value (Aki, 1965), and the  $b$ -more-incomplete (Lippiello & Petrillo, 2024) within each remaining cluster, assign these values to all earthquakes in that iteration, and repeat the workflow. The final maps represent the average of all 100 iterations, which smooths out random cluster boundaries and yields stable spatial patterns. We avoid interpreting clusters where  $M_c$  is high, since these areas are more sensitive to detection biases. Given the magnitude uncertainties and the finite number of events per cluster, we do not treat  $b$ -value differences smaller than about 0.2 as significant and focus instead on robust, large-scale patterns that are stable across different window sizes and

720 random cluster realizations. The gridded fields are obtained by interpolating the averaged  
 721 cluster values onto a regular latitude–longitude grid.

722 Figure 11 illustrates the spatial variability of the  $b$ -value and the corresponding mag-  
 723 nitude of completeness  $M_c$  for crustal (a–c) and slab-related (d–f) seismicity. For crustal  
 724 events, the classical  $b$ -value map (Figure 11a) shows values close to 1.0 along most of the  
 725 rupture, increasing to about 1.3 around Pichilemu and in parts of the southern segment,  
 726 and exceeding 1.5 in the northern onshore area where anthropogenic sources (e.g., copper  
 727 mining) and numerous small, shallow events are present. We therefore interpret much of  
 728 this high- $b$  patch as non-tectonic in origin. The  $b$ -more-incomplete estimates (Figure 11b)  
 729 retain the first-order along-strike pattern but appear smoother and less sensitive to local  
 730 variations in  $M_c$ . The crustal  $M_c$  map (Figure 11c) ranges from about 1.5 to 3.0, with  
 731 higher values offshore and in areas of sparse station coverage, and correlates strongly with  
 732 the spatial variability of the classical  $b$ -value. This correlation indicates that part of the  
 733 spatial variability in the classical  $b$ -value map reflects completeness changes rather than  
 734 genuine changes in the magnitude–frequency distribution.

735 For slab-related seismicity, classical  $b$ -values (Figure 11d) are generally lower, rang-  
 736 ing from 0.5 to 1.0 beneath the southern segment and up to approximately 1.3 beneath  
 737 Pichilemu, again following the main patterns in  $M_c$ . In contrast, the slab  $b$ -more-incomplete  
 738 map (Figure 11e) reveals a clearer along-strike segmentation, with higher  $b$ -values in the  
 739 northern part of the rupture and values close to 1.0 in the south. The slab  $M_c$  distribu-  
 740 tion (Figure 11f) is similar, with higher values where station coverage is sparse. Together,  
 741 these maps indicate that classical  $b$ -values are strongly influenced by spatial variations in  
 742  $M_c$ , whereas the  $b$ -more-incomplete estimates provide a more stable and less completeness-  
 743 biased representation of the underlying crustal and slab segmentation.

744 These spatially variable and temporally evolving  $b$ -values are consistent with the idea  
 745 that earthquake magnitude distributions reflect a dynamically evolving stress field and struc-  
 746 tural heterogeneity (Herrmann et al., 2022). Taken together, the  $b$ -more-incomplete esti-  
 747 mates highlight a pronounced along-strike contrast in  $b$ -value for crustal earthquakes, with  
 748 the highest  $b$ -values in the northern segment (~33 to 35 S) and lower  $b$ -values in the south-  
 749 ern segment (~36 to 38 S). We interpret this contrast as consistent with a weaker, fluid-  
 750 influenced plate interface in the north, where elevated pore fluid pressure ( $p_f$ ) tends to reduce  
 751 the effective normal stress ( $\sigma_{\text{eff}} = \sigma_n - p_f$ ) and favors a higher proportion of small to mod-  
 752 erate earthquakes (Schorlemmer et al., 2005; Scholz, 2015). In contrast, the lower  $b$ -values  
 753 in the south are compatible with a relatively drier, more strongly coupled interface and a  
 754 less fractured upper plate, characterized by lower pore fluid pressure and persistently high  
 755  $\sigma_{\text{eff}}$ . Classical  $b$ -value estimates remain more sensitive to spatial variations in  $M_c$ , whereas  
 756 the  $b$ -more-incomplete estimates provide a more robust and less completeness-biased view  
 757 of this segmentation.

758 Other factors, such as heterogeneous path and site effects or local variations in magni-  
 759 tude uncertainty, may also contribute to the observed patterns. This first-order north–south  
 760 contrast is, however, consistent with previous interpretations of fluid-rich versus mechani-  
 761 cally stronger domains derived from geodetic, structural, and  $b$ -value analyses (Tassara et  
 762 al., 2016; Arroyo-Solórzano & Linkimer, 2021), and is compatible with scenarios in which  
 763 fluids released from the dehydrating Nazca slab accumulate and are redistributed along the  
 764 plate interface. The strongest  $b$ -value gradients occur adjacent to the regions of highest  
 765 coseismic slip (Yue et al., 2014), consistent with stress concentration near the edges of the  
 766 main slip patches. Together, these patterns support a segmented view of the Maule rupture  
 767 and reflect the redistribution of stress, and possibly pore fluid pressure, after the  $M_w$  8.8  
 768 earthquake.

## 769 6 Conclusions

770 This study presents a high-resolution catalog of the aftershock sequence of the 2010  $M_w$   
 771 8.8 Maule earthquake in south-central Chile, covering the period from March 2010 to Jan-  
 772 uary 2011. By reanalyzing data from the IMAD seismic network with a workflow that  
 773 combines deep-learning-based detection method with relative relocation and template matching,  
 774 we identify 537,390 earthquakes, about 13 times more events than reported in previous  
 775 studies. The catalog spans magnitudes from  $M_w$  0.2 to  $M_w$  6.2, reaches a completeness level of  
 776 about  $M_w$  1.8, and resolves fine-scale seismic structures along the rupture zone, particularly  
 777 in the Pichilemu region.

778 The two estimation methods reveal markedly different temporal evolutions of the  $b$ -  
 779 value. The  $b$ -more-incomplete approach yields consistently high values throughout most  
 780 of the sequence, whereas the classical maximum likelihood estimate starts from low values  
 781 and increases with time. Despite these contrasting trends, both methods converge toward  
 782  $b \sim 1$  after roughly 270 days. This apparent stabilization may reflect a progressive transition  
 783 toward a more mature aftershock regime. However, the concurrent loss of seismic stations  
 784 during the later stages introduces uncertainty as to whether this trend represents a genuine  
 785 physical process or an artifact of decreasing detection capability.

786 Spatially, the catalog reveals a clear along-strike segmentation of  $b$ -values. Higher  $b$ -  
 787 values in the northern segment and lower values in the southern segment are consistent  
 788 with along-strike variations in effective normal stress,  $\sigma_{\text{eff}} = \sigma_n - p_f$ . Elevated pore-fluid  
 789 pressure in the north likely reduces  $\sigma_{\text{eff}}$ , promoting a higher proportion of small to moderate  
 790 earthquakes, whereas lower  $b$ -values in the south are consistent with a relatively dry, more  
 791 strongly coupled plate interface and a less fractured upper plate. Taken together with  
 792 previous geodetic and structural studies that document two main high-slip regions and  
 793 long-term forearc segmentation along the Maule margin (Moreno et al., 2010; Jara-Munoz  
 794 et al., 2015; Tassara et al., 2016), these contrasts suggest that along-strike variations in  
 795 stress, fluid pressure, and inherited structure exert a first-order control on the postseismic  
 796 evolution of the sequence.

797 This catalog provides a detailed and internally consistent dataset that enables future in-  
 798 vestigations of key physical processes governing the rupture potential and dynamic evolution  
 799 of seismicity in subduction margins. It offers opportunities to correlate seismic observations  
 800 with geodetic models (e.g., afterslip, coupling maps) and to better constrain earthquake  
 801 parameters (e.g., source contribution, attenuation parameters, site effects). In this study,  
 802 we apply this workflow to a large aftershock sequence and demonstrate that it is effec-  
 803 tive and can be used in other tectonic settings with variable data coverage and network  
 804 configurations.

## 805 Data Availability Statement

806 The complete earthquake catalog is provided both in the Supporting Information and  
 807 in the Zenodo repository described by Flores-Allende et al. (2025) (<https://doi.org/10.5281/zenodo.17858890>). The Supporting Information provides complementary  
 808 material related to the workflow, while the Zenodo repository contains the Python scripts  
 809 together with detailed instructions on how to reproduce the workflow. Seismic waveform  
 810 data were accessed online from the contributing seismic networks, and all records remain  
 811 publicly available through their corresponding data centers. The IMAD network (Beck et  
 812 al., 2014) includes the FDSN code XS (Vilotte et al., 2011), operated by CNRS-INSU and  
 813 IRIS/PASSCAL, with data publicly available at the RESIF data center (<https://doi.org/10.15778/RESIF.XS2010>). The FDSN code XY (Steve Roecker & Ray Russo, 2010) was op-  
 814 erated by GEF/SeisUK, and its data are accessible through the IRIS data center (<https://www.iris.edu/hq/>). The 3A network, also operated by GEF/SeisUK, is available via IRIS.  
 817

818 The ZE network, provided by GIPP (GFZ), can be accessed through the GEOFON data center (https://geofon.gfz.de/waveform/archive/network.php?ncode=ZE&year=2010).

820 All algorithms used in this study are open source and publicly available. The BackProjection  
 821 and Matched Filter (BPMF) workflow (Beaucé et al., 2024) is accessible at [https://github.com/ebeauche/Seismic\\_BPMF](https://github.com/ebeauche/Seismic_BPMF). The NonLinLoc-SSST-Coherence algorithm (Lomax  
 822 & Savvaidis, 2022) is available at <http://alomax.free.fr/nlloc/> and through Zenodo  
 823 (<https://zenodo.org/records/13693145>). SourceSpec (Satriano, 2021) can be found at  
 824 <https://github.com/SeismicSource/sourcespec>, and the implementation of *b*-value esti-  
 825 mation methods (Lippiello & Petrillo, 2024) is provided at [https://github.com/caccioppoli/zb\\$-more-positive](https://github.com/caccioppoli/zb$-more-positive).

826 All computations were performed using Python version 3.11.11 (Van Rossum et al.,  
 827 2007) (<https://www.python.org/>). The main scientific libraries used are ObsPy 1.4.2  
 828 (Beyreuther et al., 2010) for waveform retrieval and preprocessing (<https://doi.org/10.5281/zenodo.15309143>); SciPy 1.13.0 (Virtanen et al., 2020) for optimization and interpo-  
 829 lation (<https://scipy.org/>); and Scikit-learn 1.6.1 (Pedregosa et al., 2011) for data anal-  
 830 ysis, including clustering with HDBSCAN (McInnes et al., 2017) and MiniBatch K-means  
 831 (J. Wu, 2012) (<https://scikit-learn.org/stable/>). Figures were created using Mat-  
 832 plotlib 3.10.1 (Hunter, 2007) (<https://matplotlib.org/>), and maps were produced with  
 833 PyGMT (Wessel et al., 2019; Uieda et al., 2021) (<https://www.genericmapping-tools.org/>) and Cartopy 0.24.1 (Met Office, 2015) (<https://scitools.org.uk/cartopy/docs/latest/>). ).

### 839 Conflict of Interest Statement

840 The authors have no conflicts of interest to disclose.

### 841 Acknowledgments

842 This work was funded through the ANR-22-CPJ1-0020-01 program. E. Beaucé was  
 843 funded by the Brinson Foundation. L.F. Bonilla was funded by project ANR E-City,  
 844 AAPG 2021 – CES 22. Continuous seismic data were provided thanks to the collabora-  
 845 tive efforts of IRIS, IPGP, ENS, and GFZ. Numerical computations were conducted on the  
 846 S-CAPAD/DANTE platform at IPGP, France. We sincerely thank Sergio Ruiz and Raúl  
 847 Madariaga for their valuable discussions on seismicity in the Maule region. We also acknowl-  
 848 edge Javier Ojeda, Leoncio Cabrera, and Martin Vallée for their insightful contributions to  
 849 discussions on seismic parameters relevant to this study. Additionally, we extend our appre-  
 850 ciation to Antony Lomax, Jannes Münchmeyer, and Bertrand Potin for their constructive  
 851 feedback on the event relocation process. We also thank the Andes-FrenSZ collaboration  
 852 research program and associated researchers for their valuable comments and contributions.  
 853 Finally, we are grateful to all researchers at IPGP, Universidad de Chile, and ISTerre who  
 854 provided thoughtful insights, discussions, and feedback that contributed to improving this  
 855 study. We are very thankful to the journal editor Rachel Abercrombie, the associate ed-  
 856 tor and three anonymous reviewers for their constructive comments and suggestions that  
 857 significantly improved the quality and clarity of this work.

### 859 References

860 Agurto, H., Rietbrock, A., Ryder, I., & Miller, M. (2012). Seismic-afterslip characteriza-  
 861 tion of the 2010 mw 8.8 maule, chile, earthquake based on moment tensor inversion.  
 862 *Geophysical Research Letters*, 39(20).

863 Aki, K. (1965). Maximum likelihood estimate of *b* in the formula  $\log n = a - b m$  and its  
 864 confidence limits. *Bull. Earthquake Res. Inst., Tokyo Univ.*, 43, 237–239.

865 Allen, R. (1982). Automatic phase pickers: Their present use and future prospects. *Bulletin*  
 866 *of the Seismological Society of America*, 72(6B), S225–S242.

867 Anstey, N. A. (1964). Correlation techniques—a review. *Geophysical Prospecting*, 12(4),  
 868 355–382.

869 Aron, F., Cembrano, J., Astudillo, F., Allmendinger, R. W., & Arancibia, G. (2015).  
 870 Constructing forearc architecture over megathrust seismic cycles: Geological snapshots  
 871 from the maule earthquake region, chile. *Bulletin*, 127(3-4), 464–479.

872 Arroyo-Solórzano, M., & Linkimer, L. (2021). Spatial variability of the b-value and seismic  
 873 potential in costa rica. *Tectonophysics*, 814, 228951.

874 Båth, M. (1965). Lateral inhomogeneities of the upper mantle. *Tectonophysics*, 2(6),  
 875 483–514.

876 Beaucé, E., Frank, W. B., Paul, A., Campillo, M., & van Der Hilst, R. D. (2019). Systematic  
 877 detection of clustered seismicity beneath the southwestern alps. *Journal of Geophysical*  
 878 *Research: Solid Earth*, 124(11), 11531–11548.

879 Beaucé, E., Frank, W. B., & Romanenko, A. (2018). Fast matched filter (fmf): An effi-  
 880 cient seismic matched-filter search for both cpu and gpu architectures. *Seismological*  
 881 *Research Letters*, 89(1), 165–172.

882 Beaucé, E., Frank, W. B., Seydoux, L., Poli, P., Groebner, N., van der Hilst, R. D., &  
 883 Campillo, M. (2024). Bpmf: A backprojection and matched-filtering workflow for  
 884 automated earthquake detection and location. *Seismological Research Letters*, 95(2A),  
 885 1030–1042. Retrieved from <https://zenodo.org/records/14838292> ([Software])  
 886 doi: 10.5281/zenodo.14838292

887 Beaucé, E., van der Hilst, R. D., & Campillo, M. (2022). Microseismic constraints on the  
 888 mechanical state of the north anatolian fault zone 13 years after the 1999 m7. 4 izmit  
 889 earthquake. *Journal of Geophysical Research: Solid Earth*, 127(9), e2022JB024416.

890 Beck, S., Rietbrock, A., Tilmann, F., Barrientos, S., Meltzer, A., Oncken, O., ... Russo,  
 891 R. M. (2014). Advancing subduction zone science after a big quake. *Eos, Transactions*  
 892 *American Geophysical Union*, 95(23), 193–194. ([Dataset])

893 Beyreuther, M., Barsch, R., Krischer, L., Megies, T., Behr, Y., & Wassermann, J. (2010).  
 894 Obspy: A python toolbox for seismology. *Seismological Research Letters*, 81(3), 530–  
 895 533. Retrieved from <https://zenodo.org/records/15309143> ([Software]) doi:  
 896 10.5281/zenodo.15309143

897 Bilek, S. L., & Lay, T. (2018). Subduction zone megathrust earthquakes. *Geosphere*, 14(4),  
 898 1468–1500.

899 Bormann, P. (2012). Magnitude calibration formulas and tables, comments on their use and  
 900 complementary data. *New Manual of Seismological Observatory Practice 2 (NMSOP-2)*, 1–19. Retrieved from [https://doi.org/10.2312/GFZ.NMSOP-2\\_DS\\_3.1](https://doi.org/10.2312/GFZ.NMSOP-2_DS_3.1) (In: Bormann, P. (Ed.), *New Manual of Seismological Observatory Practice 2 (NMSOP-2)*)  
 901 doi: 10.2312/GFZ.NMSOP-2\_DS\_3.1

902 Brune, J. N. (1970). Tectonic stress and the spectra of seismic shear waves from earthquakes.  
 903 *Journal of geophysical research*, 75(26), 4997–5009.

904 Cabrera, L., Ruiz, S., Poli, P., Contreras-Reyes, E., Osses, A., & Mancini, R. (2021). North-  
 905 ern chile intermediate-depth earthquakes controlled by plate hydration. *Geophysical*  
 906 *Journal International*, 226(1), 78–90.

907 Campello, R. J., Moulavi, D., & Sander, J. (2013). Density-based clustering based on  
 908 hierarchical density estimates. In *Pacific-asia conference on knowledge discovery and*  
 909 *data mining* (pp. 160–172).

910 Campos, J., Hatzfeld, D., Madariaga, R., López, G., Kausel, E., Zollo, A., ... Lyon-Caen,  
 911 H. (2002). A seismological study of the 1835 seismic gap in south-central chile. *Physics*  
 912 *of the Earth and Planetary Interiors*, 132(1-3), 177–195.

913 Chiba, K. (2019). Spatial and temporal distributions of b-values related to long-term slow-  
 914 slip and low-frequency earthquakes in the bungo channel and hyuga-nada regions,  
 915 japan. *Tectonophysics*, 757, 1–9.

916 Collettini, C., & Tinti, E. (2025). The influence of lithology and fault source volume on  
 917 the magnitude–frequency-distribution of earthquakes. *Geophysical Research Letters*,

920 52(2), e2024GL110354.

921 Condori, C., Tavera, H., Marotta, G. S., Rocha, M. P., & Fran  a, G. S. (2017). Calibration  
922 of the local magnitude scale (ml) for per『. *Journal of Seismology*, 21(4), 987–999.

923 Cust  o, S., & Archuleta, R. (2006). b-values as a proxy for stress–inferences for dynamic  
924 modeling of the 2004 parkfield earthquake. *EOS Trans. AGU*, 87 (52), Fall Meet.  
925 *Suppl., Abstract S23C*, 167.

926 Deichmann, N. (2017). Theoretical basis for the observed break in ml/m w scaling between  
927 small and large earthquakes. *Bulletin of the Seismological Society of America*, 107(2),  
928 505–520.

929 Delouis, B., Nocquet, J.-M., & Vall  e, M. (2010). Slip distribution of the february 27, 2010  
930 mw= 8.8 maule earthquake, central chile, from static and high-rate gps, insar, and  
931 broadband teleseismic data. *Geophysical Research Letters*, 37(17).

932 Di Giacomo, D., Engdahl, E. R., & Storchak, D. A. (2018). The isc-gem earthquake  
933 catalogue (1904–2014): status after the extension project. *Earth System Science Data*,  
934 10(4), 1877–1899.

935 Essing, D., & Poli, P. (2024). Unraveling earthquake clusters composing the 2014 alto tibe-  
936 rina earthquake swarm via unsupervised learning. *Journal of Geophysical Research: Solid Earth*, 129(1), e2022JB026237.

937 Farge, G., & Brodsky, E. E. (2025). The big impact of small quakes on tectonic tremor  
938 synchronization. *Science Advances*, 11(20), eadu7173.

939 Far  as, M., Comte, D., Roecker, S., Carrizo, D., & Pardo, M. (2011). Crustal extensional  
940 faulting triggered by the 2010 chilean earthquake: The pichilemu seismic sequence.  
941 *Tectonics*, 30(6).

942 Felzer, K. R., Abercrombie, R. E., & Ekstrom, G. (2004). A common origin for aftershocks,  
943 foreshocks, and multiplets. *Bulletin of the Seismological Society of America*, 94(1),  
944 88–98.

945 Flores-Allende, R., Seydoux, L., Beauch  , E., Bonilla, L.-F., Gu  guen, P., & Satriano, C.  
946 (2025). *Repository for mw 8.8 maule aftershock deep-learning-based catalog*. Dataset.  
947 Zenodo. Retrieved from <https://doi.org/10.5281/zenodo.17858890> doi: 10.5281/  
948 zenodo.17858890

949 Folesky, J. (2024). Different earthquake nucleation conditions revealed by stress drop and  
950 b-value mapping in the northern chilean subduction zone. *Scientific Reports*, 14(1),  
951 12182.

952 Frank, W., & Shapiro, N. (2014). Automatic detection of low-frequency earthquakes (lfes)  
953 based on a beamformed network response. *Geophysical Journal International*, 197(2),  
954 1215–1223.

955 Geffers, G., Main, I., & Naylor, M. (2022). Biases in estimating b-values from small earth-  
956 quake catalogues: how high are high b-values? *Geophysical Journal International*,  
957 229(3), 1840–1855.

958 Gibbons, S. J., & Ringdal, F. (2006). The detection of low magnitude seismic events  
959 using array-based waveform correlation. *Geophysical Journal International*, 165(1),  
960 149–166.

961 Glodny, J., Echtler, H., Collao, S., Ardiles, M., Bur  n, P., & Figueroa, O. (2008). Differential  
962 late paleozoic active margin evolution in south-central chile (37° s–40° s)–the lanalhue  
963 fault zone. *Journal of South American Earth Sciences*, 26(4), 397–411.

964 Gutenberg, B., & Richter, C. F. (1944). Frequency of earthquakes in califonia. *Bulletin of  
965 the Seismological Society of America*, 34(4), 185–188.

966 Gu  guen, P., Renault, M., Bourova, E., P  quegnat, C., Cougoulat, G., Mariscal, A., ...  
967 Paul, A. (2011). Chilean aftershock network installed one week after the mw 8.8  
968 chile earthquake: Preliminary analysis of the accelerometric data. In *Poster* (p. 1).  
969 Retrieved from <http://bdsis.obs.ujf-grenoble.fr/BDs/>

970 Haberland, C., Rietbrock, A., Lange, D., Bataille, K., & Dahm, T. (2009). Structure of  
971 the seismogenic zone of the southcentral chilean margin revealed by local earthquake  
972 traveltome tomography. *Journal of Geophysical Research: Solid Earth*, 114(B1).

974 Hanks, T. C., & Kanamori, H. (1979). A moment magnitude scale. *Journal of Geophysical*  
 975 *Research: Solid Earth*, 84(B5), 2348–2350.

976 Hartigan, J. A. (1975). *Clustering algorithms*. John Wiley & Sons, Inc.

977 Hayes, G. P., Moore, G. L., Portner, D. E., Hearne, M., Flamme, H., Furtney, M., &  
 978 Smoczyk, G. M. (2018). Slab2, a comprehensive subduction zone geometry model.  
 979 *Science*, 362(6410), 58–61.

980 Herrmann, M., Piegari, E., & Marzocchi, W. (2022). Revealing the spatiotemporal complex-  
 981 ity of the magnitude distribution and b-value during an earthquake sequence. *Nature*  
 982 *Communications*, 13(1), 5087.

983 Hervé, F., Godoy, E., Parada, M. A., Ramos, V., Rapela, C., Mpodozis, C., & Davidson, J.  
 984 (1987). A general view on the chilean-argentine andes, with emphasis on their early  
 985 history. *Circum-Pacific Orogenic Belts and Evolution of the Pacific Ocean Basin*, 18,  
 986 97–113.

987 Hervé, F., Munizaga, F., Parada, M., Brook, M., Pankhurst, R., Snelling, N., & Drake,  
 988 R. (1988). Granitoids of the coast range of central chile: geochronology and geologic  
 989 setting. *Journal of South American Earth Sciences*, 1(2), 185–194.

990 Hicks, S. P., Rietbrock, A., Ryder, I. M., Lee, C.-S., & Miller, M. (2014). Anatomy of  
 991 a megathrust: The 2010 mw 8.8 maule, chile earthquake rupture zone imaged using  
 992 seismic tomography. *Earth and Planetary Science Letters*, 405, 142–155.

993 Hunter, J. D. (2007). Matplotlib: A 2d graphics environment. *Computing in Science &*  
 994 *Engineering*, 9(3), 90–95. Retrieved from <https://zenodo.org/records/15375714>  
 995 ([Software]) doi: 10.5281/zenodo.15375714

996 Jara-Munoz, J., Melnick, D., Brill, D., & Strecker, M. R. (2015). Segmentation of the 2010  
 997 maule chile earthquake rupture from a joint analysis of uplifted marine terraces and  
 998 seismic-cycle deformation patterns. *Quaternary Science Reviews*, 113, 171–192.

999 Jara-Muñoz, J., Melnick, D., Li, S., Socquet, A., Cortés-Aranda, J., Brill, D., & Strecker,  
 1000 M. (2022). The cryptic seismic potential of the pichilemu blind fault in chile revealed  
 1001 by off-fault geomorphology. *Nature Communications*, 13(1), 3371.

1002 Lange, D., Tilmann, F., Barrientos, S. E., Contreras-Reyes, E., Methe, P., Moreno, M., ...  
 1003 et al. (2012). Aftershock seismicity of the 27 february 2010 mw 8.8 maule earthquake  
 1004 rupture zone. *Earth and Planetary Science Letters*, 317, 413–425.

1005 Langston, C. A., Brazier, R., Nyblade, A. A., & Owens, T. J. (1998). Local magnitude scale  
 1006 and seismicity rate for tanzania, east africa. *Bulletin of the Seismological Society of*  
 1007 *America*, 88(3), 712–721.

1008 Li, J., Hao, M., & Cui, Z. (2024). A high-resolution aftershock catalog for the 2014 m s  
 1009 6.5 ludian (china) earthquake using deep learning methods. *Applied Sciences*, 14(5),  
 1010 1997.

1011 Lieser, K., Grevemeyer, I., Lange, D., Flueh, E., Tilmann, F., & Contreras-Reyes, E. (2014).  
 1012 Splay fault activity revealed by aftershocks of the 2010 mw 8.8 maule earthquake,  
 1013 central chile. *Geology*, 42(9), 823–826.

1014 Lippiello, E., & Petrillo, G. (2024). b-more-incomplete and b-more-positive: Insights  
 1015 on a robust estimator of magnitude distribution. *Journal of Geophysical Research: Solid*  
 1016 *Earth*, 129(2), e2023JB027849. Retrieved from <https://zenodo.org/records/8343629>  
 1017 ([Software]) doi: 10.5281/zenodo.8343629

1018 Liu, C., Lay, T., Brodsky, E. E., Dascher-Cousineau, K., & Xiong, X. (2019). Coseismic  
 1019 rupture process of the large 2019 ridgecrest earthquakes from joint inversion of geodetic  
 1020 and seismological observations. *Geophysical Research Letters*, 46(21), 11820–11829.

1021 Lomax, A. (2001). *Nonlinloc home page*.

1022 Lomax, A., Michelini, A., Curtis, A., & Meyers, R. (2009). Earthquake location, direct,  
 1023 global-search methods. *Encyclopedia of complexity and systems science*, 5, 2449–2473.

1024 Lomax, A., & Savvaidis, A. (2022). High-precision earthquake location using source-specific  
 1025 station terms and inter-event waveform similarity. *Journal of Geophysical Research: Solid*  
 1026 *Earth*, 127(1), e2021JB023190. Retrieved from <https://zenodo.org/records/13693145>  
 1027 ([Software]) doi: 10.5281/zenodo.13693145

1028 Lorito, S., Romano, F., Atzori, S., Tong, X., Avallone, A., McCloskey, J., ... Piatanesi, A.

1029 (2011). Limited overlap between the seismic gap and coseismic slip of the great 2010  
 1030 chile earthquake. *Nature Geoscience*, 4(3), 173–177.

1031 Madariaga, R., Métois, M., Vigny, C., & Campos, J. (2010). Central chile finally breaks.  
 1032 *Science*, 328(5975), 181–182.

1033 Mancini, S., Segou, M., Werner, M. J., Parsons, T., Beroza, G., & Chiaraluce, L. (2022). On  
 1034 the use of high-resolution and deep-learning seismic catalogs for short-term earthquake  
 1035 forecasts: Potential benefits and current limitations. *Journal of Geophysical Research: Solid*  
 1036 *Earth*, 127(11), e2022JB025202.

1037 Marsan, D. (2005). The role of small earthquakes in redistributing crustal elastic stress.  
 1038 *Geophysical Journal International*, 163(1), 141–151.

1039 McInnes, L., Healy, J., Astels, S., & et al. (2017). hdbscan: Hierarchical density based  
 1040 clustering. *J. Open Source Softw.*, 2(11), 205.

1041 Melnick, D., Bookhagen, B., Strecker, M. R., & Echtler, H. P. (2009). Segmentation  
 1042 of megathrust rupture zones from fore-arc deformation patterns over hundreds to  
 1043 millions of years, arauco peninsula, chile. *Journal of Geophysical Research: Solid*  
 1044 *Earth*, 114(B1).

1045 Met Office. (2015). Cartopy: A cartographic python library with a matplotlib interface  
 1046 [Computer software manual]. Exeter, UK. Retrieved from <https://zenodo.org/records/13905945> ([Software]) doi: 10.5281/zenodo.13905945

1047 Minetto, R., Helmstetter, A., Schwartz, S., Langlais, M., Nomade, J., & Guéguen, P. (2022).  
 1048 Analysis of the spatiotemporal evolution of the maurienne swarm (french alps) based  
 1049 on earthquake clustering. *Earth and Space Science*, 9(7), e2021EA002097.

1050 Moreno, M., Rosenau, M., & Oncken, O. (2010). 2010 maule earthquake slip correlates with  
 1051 pre-seismic locking of andean subduction zone. *Nature*, 467(7312), 198–202.

1052 Moscoso, E. I., & Contreras-Reyes, E. (2012). Outer rise seismicity related to the maule,  
 1053 chile 2010 mega-thrust earthquake and hydration of the incoming oceanic lithosphere.  
 1054 *Andean Geology*, 39(3), 564–572.

1055 Mousavi, S. M., & Beroza, G. C. (2023). Machine learning in earthquake seismology. *Annual*  
 1056 *Review of Earth and Planetary Sciences*, 51(1), 105–129.

1057 Mpodozis, C., & Ramos, V. (1990). The andes of chile and argentina. *Circum Pacific*  
 1058 *Council Publications*, 11, 59–90.

1059 Neighbors, C., Liao, E., Cochran, E. S., Funning, G., Chung, A., Lawrence, J., ...  
 1060 Andrés Sepulveda, H. (2015). Investigation of the high-frequency attenuation parameter,  
 1061 kappa, from aftershocks of the 2010 m w 8.8 maule, chile earthquake. *Geophysical*  
 1062 *Journal International*, 200(1), 200–215.

1063 Ojeda, J., Ruiz, S., del Campo, F., & Carvajal, M. (2020). The 21 may 1960 mw 8.1  
 1064 concepción earthquake: A deep megathrust foreshock that started the 1960 central-  
 1065 south chilean seismic sequence. *Seismological Research Letters*, 91(3), 1617–1627.

1066 Pedregosa, F., Varoquaux, G., Gramfort, A., et al. (2011). Scikit-learn: Machine  
 1067 learning in python. *Journal of Machine Learning Research*, 12, 2825–2830. Retrieved  
 1068 from <https://zenodo.org/records/14627164> ([Software]) doi: 10.5281/zenodo.14627164

1069 Peng, Z., & Zhao, P. (2009). Migration of early aftershocks following the 2004 parkfield  
 1070 earthquake. *Nature Geoscience*, 2(12), 877–881.

1071 Piquer, J., Yáñez, G., Rivera, O., & Cooke, D. (2019). Long-lived crustal damage zones  
 1072 associated with fault intersections in the high andes of central chile. *Andean Geology*.

1073 Pollitz, F. F., Brooks, B., Tong, X., Bevis, M. G., Foster, J. H., Bürgmann, R., ... others  
 1074 (2011). Coseismic slip distribution of the february 27, 2010 mw 8.8 maule, chile  
 1075 earthquake. *Geophysical Research Letters*, 38(9).

1076 Potin, B., Ruiz, S., Aden-Antoniow, F., Madariaga, R., & Barrientos, S. (2025). A revised  
 1077 chilean seismic catalog from 1982 to mid-2020. *Seismological Research Letters*, 96(1),  
 1078 484–498.

1079 Richter, C. F. (1935). An instrumental earthquake magnitude scale. *Bulletin of the Seis-*  
 1080 *ological Society of America*, 25(1), 1–32.

1081 Rietbrock, A., Ryder, I., Hayes, G., Haberland, C., Comte, D., Roecker, S., & Lyon-Caen,  
 1082

1084 H. (2012). Aftershock seismicity of the 2010 maule mw= 8.8, chile, earthquake:  
 1085 Correlation between co-seismic slip models and aftershock distribution? *Geophysical*  
 1086 *Research Letters*, 39(8).

1087 Ross, Z. E., Idini, B., Jia, Z., Stephenson, O. L., Zhong, M., Wang, X., ... et al. (2019). Hi-  
 1088 erarchical interlocked orthogonal faulting in the 2019 ridgecrest earthquake sequence.  
 1089 *Science*, 366(6463), 346–351.

1090 Ruegg, J., Rudloff, A., Vigny, C., Madariaga, R., De Chabalier, J., Campos, J., ... Dimitrov,  
 1091 D. (2009). Interseismic strain accumulation measured by gps in the seismic gap  
 1092 between constitución and concepción in chile. *Physics of the Earth and Planetary*  
 1093 *Interiors*, 175(1-2), 78–85.

1094 Ruiz, J. A., & Contreras-Reyes, E. (2015). Outer rise seismicity boosted by the maule 2010  
 1095 mw 8.8 megathrust earthquake. *Tectonophysics*, 653, 127–139.

1096 Ruiz, J. A., Hayes, G. P., Carrizo, D., Kanamori, H., Socquet, A., & Comte, D. (2014).  
 1097 Seismological analyses of the 2010 march 11, pichilemu, chile m w 7.0 and m w 6.9  
 1098 coastal intraplate earthquakes. *Geophysical Journal International*, 197(1), 414–434.

1099 Ruiz, S., Aden-Antoniow, F., Baez, J. C., Otarola, C., Potin, B., del Campo, F., ...  
 1100 Bernard, P. (2017). Nucleation phase and dynamic inversion of the mw 6.9 val-  
 1101 paraíso 2017 earthquake in central chile. *Geophysical Research Letters*, 44(20),  
 1102 10,290-10,297. Retrieved from <https://agupubs.onlinelibrary.wiley.com/doi/abs/10.1002/2017GL075675> doi: <https://doi.org/10.1002/2017GL075675>

1103 Ruiz, S., & Madariaga, R. (2018). Historical and recent large megathrust earthquakes in  
 1104 chile. *Tectonophysics*, 733, 37–56.

1105 Ruiz, S., Madariaga, R., Astroza, M., Saragomi, G. R., Lancieri, M., Vigny, C., & Campos,  
 1106 J. (2012). Short-period rupture process of the 2010 mw 8.8 maule earthquake in chile.  
 1107 *Earthquake Spectra*, 28(1\_suppl1), 1–18.

1108 Ryder, I., Rietbrock, A., Kelson, K., Bürgmann, R., Floyd, M., Socquet, A., ... Carrizo,  
 1109 D. (2012). Large extensional aftershocks in the continental forearc triggered by the  
 1110 2010 maule earthquake, chile. *Geophysical Journal International*, 188(3), 879–890.

1111 Salazar, K., & McNutt, M. (2011). Report on the 2010 chilean earthquake and tsunami  
 1112 response. *Reston, Virginia: US Geological Survey*.

1113 Santibáñez, I., Cembrano, J., García-Pérez, T., Costa, C., Yáñez, G., Marquardt, C., ...  
 1114 González, G. (2019). Crustal faults in the chilean andes: geological constraints and  
 1115 seismic potential. *Andean Geology*, 46(1), 32–65.

1116 Satriano, C. (2021). Sourcespec–earthquake source parameters from s-wave displacement  
 1117 spectra. *Zenodo*. Retrieved from <https://zenodo.org/records/6954238> ([Soft-  
 1118 ware]) doi: 10.5281/zenodo.6954238

1119 Scholz, C. H. (2015). On the stress dependence of the earthquake b value. *Geophysical*  
 1120 *Research Letters*, 42(5), 1399–1402.

1121 Schorlemmer, D., Wiemer, S., & Wyss, M. (2005). Variations in earthquake-size distribution  
 1122 across different stress regimes. *Nature*, 437(7058), 539–542.

1123 Sculley, D. (2010). Web-scale k-means clustering. In *Proceedings of the 19th international*  
 1124 *conference on world wide web* (pp. 1177–1178).

1125 Shelly, D. R., Beroza, G. C., & Ide, S. (2007). Non-volcanic tremor and low-frequency  
 1126 earthquake swarms. *Nature*, 446(7133), 305–307.

1127 Skoumal, R. J., Brudzinski, M. R., Currie, B. S., & Levy, J. (2014). Optimizing multi-  
 1128 station earthquake template matching through re-examination of the youngstown,  
 1129 ohio, sequence. *Earth and Planetary Science Letters*, 405, 274–280.

1130 Steve Roecker, & Ray Russo. (2010). *Ramp response for 2010 chile earthquake*. International  
 1131 Federation of Digital Seismograph Networks. Retrieved from [https://doi.org/10.7914/SN/XY\\_2010](https://doi.org/10.7914/SN/XY_2010) ([Dataset]) doi: 10.7914/SN/XY\_2010

1132 Tan, Y. J., Waldhauser, F., Ellsworth, W. L., Zhang, M., Zhu, W., Michele, M., ... Segou,  
 1133 M. (2021). Machine-learning-based high-resolution earthquake catalog reveals how  
 1134 complex fault structures were activated during the 2016–2017 central italy sequence.  
 1135 *The Seismic Record*, 1(1), 11–19.

1136 Tassara, A., Soto, H., Bedford, J., Moreno, M., & Baez, J. C. (2016). Contrasting amount

1139 of fluids along the megathrust ruptured by the 2010 maule earthquake as revealed by  
 1140 a combined analysis of aftershocks and afterslip. *Tectonophysics*, *671*, 95–109.

1141 Trugman, D. T., & Shearer, P. M. (2017). Growclust: A hierarchical clustering algorithm  
 1142 for relative earthquake relocation, with application to the spanish springs and sheldon,  
 1143 nevada, earthquake sequences. *Seismological Research Letters*, *88*(2A), 379–391.

1144 Uieda, L., et al. (2021). Pygmt: A python interface for the generic mapping tools. *SoftwareX*,  
 1145 *15*, 100703. Retrieved from <https://zenodo.org/records/4592991> ([Software]) doi:  
 1146 10.5281/zenodo.4592991

1147 van der Elst, N. J. (2021). B-positive: A robust estimator of aftershock magnitude dis-  
 1148 tribution in transiently incomplete catalogs. *Journal of Geophysical Research: Solid*  
 1149 *Earth*, *126*(2), e2020JB021027.

1150 Van Rossum, G., et al. (2007). Python programming language. In *Usenix annual technical*  
 1151 *conference* (Vol. 41, pp. 1–36). Retrieved from <https://www.python.org/downloads/release/python-31111/> ([Software])

1152 Vigny, C., Socquet, A., Peyrat, S., Ruegg, J.-C., Métois, M., Madariaga, R., ... et al.  
 1153 (2011). The 2010 mw 8.8 maule megathrust earthquake of central chile, monitored by  
 1154 gps. *Science*, *332*(6036), 1417–1421.

1155 Villette, J., et al. (2011). Seismic network xs: Chile maule aftershock temporary experiment  
 1156 (resif-sismob). *RESIF-Réseau Sismologique et géodésique Français*.

1157 Virtanen, P., Gommers, R., Oliphant, T. E., et al. (2020). Scipy 1.0: Fundamental al-  
 1158 gorithms for scientific computing in python. *Nature Methods*, *17*, 261–272. Re-  
 1159 trieval from <https://zenodo.org/records/10840233> ([Software]) doi: 10.5281/  
 1160 zenodo.10840233

1161 Waldhauser, F. (2001). hypodd—a program to compute double-difference hypocenter loca-  
 1162 tions (hypodd version 1.0-03/2001). *US Geol. Surv. Open File Rep.*, *01*, 113.

1163 Wessel, P., Luis, J., Uieda, L., et al. (2019). The generic mapping tools version 6 [software].  
 1164 *Geochemistry, Geophysics, Geosystems*, *20*(11), 5556–5564. Retrieved from <https://zenodo.org/records/3407866> ([Software]) doi: 10.5281/zenodo.3407866

1165 White, M. C., Fang, H., Nakata, N., & Ben-Zion, Y. (2020). Pykonal: a python package  
 1166 for solving the eikonal equation in spherical and cartesian coordinates using the fast  
 1167 marching method. *Seismological Research Letters*, *91*(4), 2378–2389.

1168 Wu, J. (2012). *Advances in k-means clustering: a data mining thinking*. Springer Science  
 1169 & Business Media. Retrieved from <https://scikit-learn.org/stable/modules/generated/sklearn.cluster.MiniBatchKMeans.html> ([Software])

1170 Wu, Y.-M., Allen, R. M., & Wu, C.-F. (2005). Revised ml determination for crustal  
 1171 earthquakes in taiwan. *Bulletin of the Seismological Society of America*, *95*(6), 2517–  
 1172 2524.

1173 Yao, D., Walter, J. I., Meng, X., Hobbs, T. E., Peng, Z., Newman, A. V., ... Protti,  
 1174 M. (2017). Detailed spatiotemporal evolution of microseismicity and repeating earth-  
 1175 quakes following the 2012 mw 7.6 nicoya earthquake. *Journal of Geophysical Research: Solid*  
 1176 *Earth*, *122*(1), 524–542.

1177 Yue, H., Lay, T., Rivera, L., An, C., Vigny, C., Tong, X., & Baez Soto, J. C. (2014).  
 1178 Localized fault slip to the trench in the 2010 maule, chile mw= 8.8 earthquake from  
 1179 joint inversion of high-rate gps, teleseismic body waves, insar, campaign gps, and  
 1180 tsunami observations. *Journal of Geophysical Research: Solid Earth*, *119*(10), 7786–  
 1181 7804.

1182 Zhu, W., & Beroza, G. C. (2019). Phasenet: a deep-neural-network-based seismic arrival-  
 1183 time picking method. *Geophysical Journal International*, *216*(1), 261–273.

1184